JrnlID 10444_ArtID 09921_Proof#1 - 16/01/2022
Adv Comput Math _####################_
https://doi.org/10.1007/s10444-021-09921-3

Improvement of hierarchical matrices for 3D elastodynamic problems with a complex wavenumber

Laura Bagur[1] · Stéphanie Chaillat[1] · Patrick Ciarlet Jr.[1]

Received: 16 June 2021 / Accepted: 13 December 2021

Abstract

It is well known in the literature that standard hierarchical matrix ($\mathcal{H}$-matrix)-based methods, although very efficient for asymptotically smooth kernels, are not optimal for oscillatory kernels. In a previous paper, we have shown that the method should nevertheless be used in the mechanical engineering community due to its still important data compression rate and its straightforward implementation compared to $\mathcal{H}^2$-matrix, or directional, approaches. Since in practice, not all materials are purely elastic, it is important to be able to consider visco-elastic cases. In this context, we study the effect of the introduction of a complex wavenumber on the accuracy and efficiency of $\mathcal{H}$-matrix-based fast methods for solving dense linear systems arising from the discretization of the elastodynamic (and Helmholtz) Green's tensors. Interestingly, such configurations are also encountered in the context of the solution of transient purely elastic problems with the convolution quadrature method. Relying on the theory proposed in Börm et al. (*IMA Journal of Numerical Analysis* 12, 2020) for $\mathcal{H}^2$-matrices for Helmholtz problems, we study the influence of the introduction of damping on the data compression rate of standard $\mathcal{H}$-matrices. We propose an improvement of $\mathcal{H}$-matrix-based fast methods for this kind of configuration and illustrate how the introduction of a complex wavenumber can, as expected, improve further the efficiency of such methods. This work is complementary to the recent report (Börm et al., *IMA Journal of Numerical Analysis* 12, 2020). Here, in addition to addressing another physical problem, we consider standard $\mathcal{H}$-matrices, derive a simple criterion to introduce additional compression and we perform extensive numerical experiments.

Communicated by: Michael O'Neil

This article belongs to the Topical Collection: *Advances in Computational Integral Equations*
Guest Editors: Stephanie Chaillat, Adrianna Gillman, Per-Gunnar Martinsson, Michael O'Neil, Mary-Catherine Kropinski, Timo Betcke, Alex Barnett

✉ Stéphanie Chaillat
stephanie.chaillat@ensta-paris.fr

Extended author information available on the last page of the article.

Keywords Hierachical matrices · Convolution quadrature method · Boundary element method · (Visco)-Elastodynamics

Mathematics Subject Classification (2010)

1 Introduction

The 3D linear isotropic elastodynamic equation for the displacement field $\boldsymbol{u}$ (also called Navier equation) is given by

$$\operatorname{div}\sigma(\boldsymbol{u}) + \rho\omega^2\boldsymbol{u} = 0 \tag{1}$$

where $\omega > 0$ is the circular frequency. It is supplemented with appropriate boundary conditions which contain the data. The stress and strain tensors are respectively given by $\sigma(\boldsymbol{u}) = \lambda(\operatorname{div}\boldsymbol{u})\mathbf{I}_3 + 2\mu\varepsilon(\boldsymbol{u})$ and $\varepsilon(\boldsymbol{u}) = \frac{1}{2}\left([\nabla\boldsymbol{u}] + [\nabla\boldsymbol{u}]^{\mathsf{T}}\right)$, where $\mathbf{I}_3$ is the 3-by-3 identity matrix and $[\nabla\boldsymbol{u}]$ is the 3-by-3 matrix whose β-th column is the gradient of the β-th component of $\boldsymbol{u}$ for $1 \le \beta \le 3$, μ and λ are the Lamé parameters and ρ is the density. Denoting $k_p^2 = \rho\omega^2(\lambda + 2\mu)^{-1}$ and $k_s^2 = \rho\omega^2\mu^{-1}$ the so-called P and S wavenumbers, the Green's tensor of the Navier equation is a 3-by-3 matrix-valued function expressed by

$$\mathbf{U}_\omega(\boldsymbol{x}, \boldsymbol{y}) = \frac{1}{\rho\omega^2}\left(\boldsymbol{curl}\,\boldsymbol{curl}_{\boldsymbol{x}}\left[\frac{e^{ik_s|\boldsymbol{x}-\boldsymbol{y}|}}{4\pi|\boldsymbol{x}-\boldsymbol{y}|}\mathbf{I}_3\right] - \nabla_{\boldsymbol{x}}\mathbf{div}_{\boldsymbol{x}}\left[\frac{e^{ik_p|\boldsymbol{x}-\boldsymbol{y}|}}{4\pi|\boldsymbol{x}-\boldsymbol{y}|}\mathbf{I}_3\right]\right) \tag{2}$$

where the index $\boldsymbol{x}$ means that differentiation is carried out with respect to $\boldsymbol{x}$ and $\mathbf{div}_{\boldsymbol{x}}\mathbb{A}$ corresponds to the application of the divergence along each row of $\mathbb{A}$. One may use this tensor to represent the solution of (1). Alternately, one may use the tensor $\mathbf{T}_\omega(\boldsymbol{x}, \boldsymbol{y})$, which is obtained by applying the traction operator

$$\boldsymbol{T} = 2\mu\frac{\partial}{\partial\boldsymbol{n}} + \lambda\boldsymbol{n}\operatorname{div} + \mu\,\boldsymbol{n}\times\boldsymbol{curl} \tag{3}$$

to each column of $\mathbf{U}_\omega(\boldsymbol{x}, \boldsymbol{y})$: $\mathbf{T}_\omega(\boldsymbol{x}, \boldsymbol{y}) = [\boldsymbol{T}_{\boldsymbol{y}}\mathbf{U}_\omega(\boldsymbol{x}, \boldsymbol{y})]$ where the index $\boldsymbol{y}$ means that differentiation is carried out with respect to $\boldsymbol{y}$.

We consider the fast solution of dense linear systems of the form

$$\mathbb{A}\mathbf{p} = \mathbf{b}, \quad \mathbb{A} \in \mathbb{C}^{3N_c\times 3N_c} \tag{4}$$

where $\mathbb{A}$ is the matrix corresponding to the discretization of the 3-by-3 Green's tensors $\mathbf{U}_\omega(\boldsymbol{x}_i, \boldsymbol{y}_j)$ or $\mathbf{T}_\omega(\boldsymbol{x}_i, \boldsymbol{y}_j)$ for two clouds of N_c points $(\boldsymbol{x}_i)_{1\le i\le N_c}$ and $(\boldsymbol{y}_j)_{1\le j\le N_c}$. Here $\mathbf{p}$ is the unknown vector approximating the solution at $(\boldsymbol{x}_i)_{1\le i\le N_c}$ and $\mathbf{b}$ is a given right hand side that depends on the data. Such dense systems are encountered for example in the context of the Boundary Element Method (with a straightforward derivation for piecewise constant interpolation of the unknown field) [5, 33].

If no compression or acceleration technique is used, the storage of such a system is of the order $O(N_c^2)$, the iterative solution (e.g., with GMRES) is $O(N_{\text{iter}}N_c^2)$ where N_{iter} is the number of iterations, while the direct solution (e.g., via LU factorizations) is $O(N_c^3)$. In the last decades, different approaches have been proposed to speed up

the solution of dense systems. The most well-known method is probably the fast multipole method (FMM) proposed by Greengard and Rokhlin [21] which enables a fast evaluation of the matrix-vector products. We recall that the matrix-vector product is the crucial tool in the context of an iterative solution. Initially developed for N-body simulations, the FMM has then been extended to oscillatory kernels [16, 20]. The method is now widely used in many application fields and has shown its capabilities in the context of mechanical engineering problems solved with the BEM [13, 25, 37].

An alternative approach designed for dense systems is based on the concept of hierarchical matrices ($\mathcal{H}$-matrices) [2]. The principle of $\mathcal{H}$-matrices is to partition the initial dense linear system, and then approximate it into a data-sparse one, by finding sub-blocks in the matrix that can be accurately estimated by low-rank matrices. In other terms, one further approximates the matrix $\mathbb{A}$ from (4). The efficiency of hierarchical matrices relies on the possibility to approximate, under certain conditions, the underlying kernel function by low-rank matrices. The approach has been shown to be very efficient for asymptotically smooth kernels (e.g., Laplace kernel). On the other hand, oscillatory kernels such as the Helmholtz or elastodynamic kernels, are not asymptotically smooth. In these cases, the method is not optimal [1]. To avoid the increase of the rank for high-frequency problems, $\mathcal{H}^2$-matrix, or directional, methods have been proposed [6, 7]. $\mathcal{H}^2$-matrices are a specialization of hierarchical matrices. It is a multigrid-like version of $\mathcal{H}$-matrices that enables more compression, by factorizing some basis functions of the approximate separable expansion.

Since the implementation of $\mathcal{H}^2$-matrix methods is much more involved than the one of the standard $\mathcal{H}$-matrix, in [14] we have studied the frequency-range within which the $\mathcal{H}$-matrices are efficient for elastodynamic problems and what can be expected of such an approach to solve problems encountered in mechanical engineering. We have shown that even though the method is not optimal (in the sense that more efficient approaches can be proposed at the cost of a much more complex implementation effort), an efficient solver is easily developed. The capabilities of the method have been illustrated on numerical examples using the Boundary Element Method.

In practice, not all materials are purely elastic and it is thus important to be able to consider visco-elastic cases. In this context, we study the effect of the introduction of a complex wavenumber on the accuracy and efficiency of hierarchical matrix ($\mathcal{H}$-matrix)-based fast methods for solving dense linear systems arising from the discretization of the elastodynamic Green's tensors. Interestingly, such configurations are also encountered in the context of the solution of transient purely elastic problems with the convolution quadrature method. Relying on the theory proposed in [12] for $\mathcal{H}^2$-matrices for Helmholtz problems, we study the influence of the introduction of damping on the data compression rate of standard $\mathcal{H}$-matrices. We propose an improvement of $\mathcal{H}$-matrix-based fast methods for this kind of configuration and illustrate how the introduction of a complex wavenumber can, as expected, improve further the efficiency of such methods. This work is complementary to the recent report [12]. Here, in addition to addressing another physical problem, we consider standard $\mathcal{H}$-matrices, derive an additional condition to obtain more compression and we perform extensive numerical experiments.

This paper is organized as follows. In Section 2, we recall the main algorithmic components of standard $\mathcal{H}$-matrices. Then in Section 3, we review existing and

improved admissibility conditions for the case of complex wavenumbers. We discuss the similarities, differences and novelties compared to [12]. In Section 4, we perform extensive numerical tests to show the efficiency of a new admissibility condition, designed to improve the efficiency of standard $\mathcal{H}$-matrices in the case of complex wavenumbers. Section 5 is devoted to the discussion of some practical situations in which this improved approach will be useful. The paper ends with some conclusions and future works.

2 Main components of $\mathcal{H}$-matrices

Hierarchical matrices or $\mathcal{H}$-matrices have been introduced by Hackbusch [22] to compute a data-sparse representation of some special dense matrices (e.g., matrices resulting from the discretization of non-local operators). The principle of $\mathcal{H}$-matrices is (i) to partition the matrix into blocks and (ii) to perform low-rank approximations of the blocks of the matrix which are known a priori (by using an admissibility condition) to be accurately approximated by low-rank decompositions. With these two ingredients it is possible to define fast iterative and direct solvers for matrices having a hierarchical representation. Using low-rank representations, the memory requirements and costs of a matrix-vector product are reduced. In addition, using $\mathcal{H}$-matrix arithmetic it is possible to derive fast direct solvers.

Clustering of the unknowns The key ingredient of hierarchical matrices is the recursive block subdivision (Fig. 1). The first step, prior to the partition of the matrix, is thus a partitioning based on the geometry of the set of row and column indices of the matrix $\mathbb{A}$. The purpose is to perform a permutation of the indices in the matrix to reflect the physical distance and thus interaction between degrees of freedom. Consecutive indices should correspond to DOFs that interact at close range. For the sake of clarity, in this work $\mathbb{A}$ is defined by the same set of indices $I = \{1, \ldots, n\}$ for rows and columns. A binary tree $\mathcal{T}_I$ is used to drive the clustering. Each node of the tree

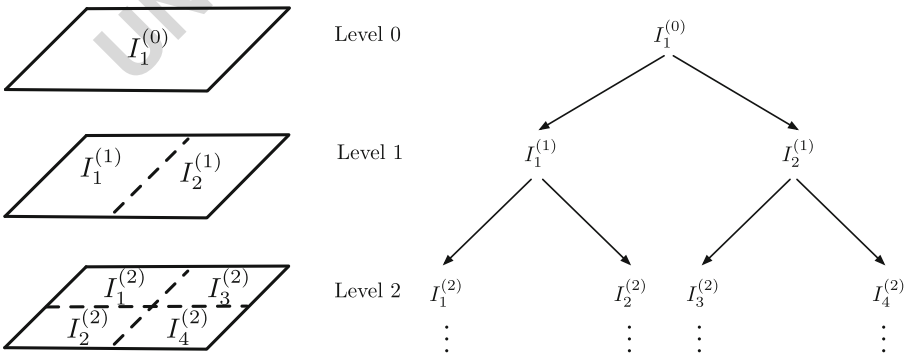

(a) Partition of the physical domain (b) Binary cluster tree $\mathcal{T}_I$

Fig. 1 Illustration of the clustering of the degrees of freedom: (a) partition of the degrees of freedom in the domain and (b) corresponding binary tree

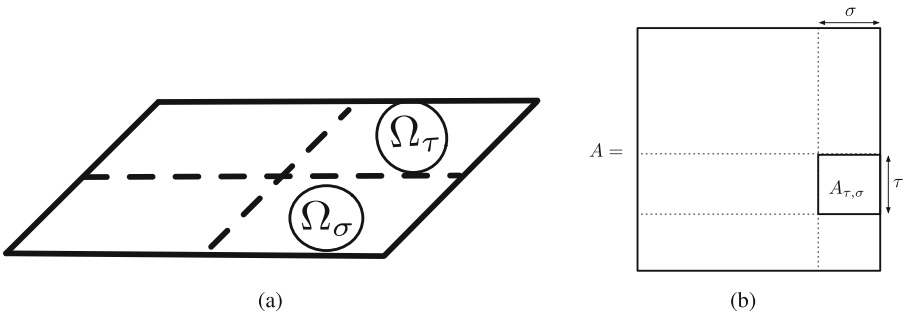

Fig. 2 Illustration of the construction of the block cluster tree: (a) clustering of the unknowns on the geometry and (b) corresponding block clustering in the matrix

defines a subset of indices $\sigma \subset I$ and each subset corresponds to a part in the partition of the domain. There exist different approaches to perform the subdivision [23]. We consider the simplest possible one : based on a geometric argument. For each node in the tree, we determine the box enclosing all the points in the cloud and subdivide it into two balanced boxes, along the largest dimension. The subdivision is stopped when a prescribed number of points per box N_{leaf}, is reached. The depth of the tree $\mathcal{T}_I$ is denoted by $L(I)$.

Subdivision of the matrix After the clustering of the unknowns is performed, a block cluster representation $\mathcal{T}_{I\times I}$ of the matrix $\mathbb{A}$ is defined by going through the cluster tree $\mathcal{T}_I$. Each node of $\mathcal{T}_{I\times I}$ contains a pair (σ, τ) of indices of $\mathcal{T}_I$ and defines a block of $\mathbb{A}$ (see Fig. 2). This uniform partition defines a block structure of the matrix with a full pattern of $4^{L(I)-1}$ blocks, in particular every node of the tree at the leaf level is connected with all the other nodes at the leaf level (Fig. 3a). This partition

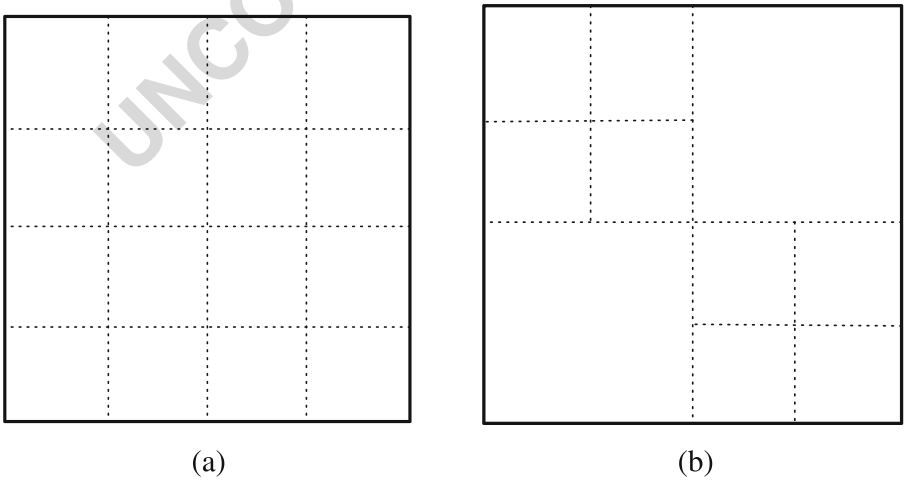

Fig. 3 (a) Block cluster representation $\mathcal{T}_{I\times I}$ for the illustrative example (full structure). (b) Hierarchical partition $\mathcal{P} \subset \mathcal{T}_{I\times I}$ of the same matrix based on the admissibility condition (sparse structure)

is not optimal since some parts of the matrix $\mathbb{A}$ can accurately be approximated by a low-rank matrix at a higher level (i.e., for larger clusters). Such blocks are said to be *admissible*. A hierarchical representation $\mathcal{P} \subset \mathcal{T}_{I\times I}$ that uses the cluster tree $\mathcal{T}_I$ and the existence of *admissible* blocks is more appropriate. Starting from the initial matrix, each block is recursively subdivided until it is either *admissible* or the leaf level is reached. For complex 3D geometries, an admissibility condition based on the geometry and the interaction distance between points is used to determine a priori the *admissible* blocks. For more details on the construction of the block cluster tree, we refer the interested reader to [9]. The partition $\mathcal{P}$ is subdivided into two subsets $\mathcal{P}^{\text{ad}}$ and $\mathcal{P}^{\text{non-ad}}$ reflecting the possibility for a block $\tau \times \sigma$ to be either *admissible*, i.e., $\tau \times \sigma \in \mathcal{P}^{\text{ad}}$; or *non-admissible*, i.e., $\tau \times \sigma \in \mathcal{P}^{\text{non-ad}}$. It is clear that $\mathcal{P} = \mathcal{P}^{\text{ad}} \cup \mathcal{P}^{\text{non-ad}}$. To sum up, the blocks of the partition can be of three types: at the leaf level a block can be either an *admissible* block or a *non-admissible* block, at a non-leaf level a block can be either an *admissible* block or an $\mathcal{H}$-matrix (i.e., a block that will be subsequently hierarchically subdivided).

Performing low-rank approximations Once the *admissible* blocks are determined, an accurate rank-revealing algorithm is applied to determine low-rank approximations. We recall that the numerical rank of a matrix $\mathbb{A}$ is

$$r(\varepsilon) := \min\{r \mid ||\mathbb{A} - \mathbb{A}_r|| \leq \varepsilon ||\mathbb{A}||\} \tag{5}$$

where $\mathbb{A}_r$ defines the singular value decomposition (SVD) of $\mathbb{A}$ keeping only the r largest singular values and $\varepsilon > 0$ is a given parameter. Such an algorithm must be accurate (i.e., its result, the computed numerical rank, must be as small as possible) to avoid unnecessary computational costs. The truncated Singular Value Decomposition (SVD) [17] gives the best low-rank approximation (Eckart-Young theorem) for unitary invariant norms (e.g., Frobenius or spectral norm). Thus, it produces an approximation with the smallest possible numerical rank for a given prescribed accuracy. But the computation of the SVD is expensive, i.e., in the order of $O(\max(m,n) \times \min(m,n)^2)$ for an $m \times n$ matrix, and in addition it requires the computation of all the entries of $\mathbb{A}$. In the context of the $\mathcal{H}$-matrices, the use of the SVD would induce the undesired need to assemble the complete matrix.

The adaptive cross approximation (ACA) [3, 4] offers an interesting alternative to the SVD since it produces a quasi-optimal low-rank approximation without requiring the assembly of the complete matrix. The starting point of the ACA is that every matrix of rank r is the sum of r matrices of rank 1. The ACA is thus a greedy algorithm that improves the accuracy of the approximation by adding iteratively rank-1 matrices. There are various ACAs that differ by the choice of the best pivot at each iteration. The simplest approach is the so-called fully pivoted ACA and it consists in choosing the pivot as the largest entry in the residual. But similarly to the SVD, it requires the computation of all the entries of $\mathbb{A}$ to compute the pivot indices. It is not an interesting option for the construction of $\mathcal{H}$-matrices. The partially pivoted ACA proposes an alternative approach to choose the pivot avoiding the assembly of the complete matrix. The idea is to maximize alternately the residual for only one of the two indices and to keep the other one fixed. With this strategy, only one row and one column is assembled at each iteration. The complexity of the partially pivoted

ACA is reduced to $O(r_{\mathrm{ACA}}^2(m+n))$, where r_{ACA} is the achieved rank. This is the approach used in this work but the results presented do not depend on this choice. Other approaches such as fast multipole expansions [21, 31], panel clustering [24, 32], quadrature formulas [8] or interpolations [30] could be used. The advantages of the ACA are to be purely algebraic and easy to implement.

3 Existing admissibility conditions and improvements for the case of complex wavenumbers

The admissibility condition enables to distinguish blocks which are known a priori to be accurately approximated by a low-rank approximation. The standard admissibility condition for $\mathcal{H}$-matrices, optimal for asymptotically smooth kernels and efficient for oscillatory kernels is given by

$$\text{the block } X \times Y \text{ is admissible if } \min(\mathrm{diam}(X), \mathrm{diam}(Y)) \leq \eta\, \mathrm{dist}(X, Y) \tag{6}$$

with $\mathrm{diam}(X)$, the diameter of the cluster X (in practice the diameter of the bounding box), and $\mathrm{dist}(X, Y)$, the minimal distance between points on clusters X and Y (the distance between the bounding boxes in practice) (see Fig. 4). Following the analysis detailed in [14], we will set $\eta = 3$.

Sparsification condition for damped kernels In the context of oscillatory kernels with complex wavenumbers, we know that $\frac{\exp(ik_\beta r)}{r}$ is the dominant term of the 3D elastodynamic kernel function. A first issue is thus to determine when the negative exponential term introduced in the kernel, due to $Im(k_\beta) > 0$ (with $\beta = s$ or p), dominates the oscillatory behavior. For a given wavenumber $k_\beta \in \mathbb{C}$ with $Im(k_\beta) > 0$, the question thus reduces to find the smallest value $r_{lim} > 0$ such that:

$$\forall r \geq r_{lim}, \left|\frac{\exp(ik_\beta r)}{r}\right| \leqslant \varepsilon_{decay} \left|\frac{\exp(ik_\beta r_{min})}{r_{min}}\right| \tag{7}$$

In (7), there are two parameters:

– r_{min}, which is related to the mesh. It can be defined for example as the minimal distance between two nodes of the boundary element mesh (importantly it is thus also related to the minimal distance between two clusters).

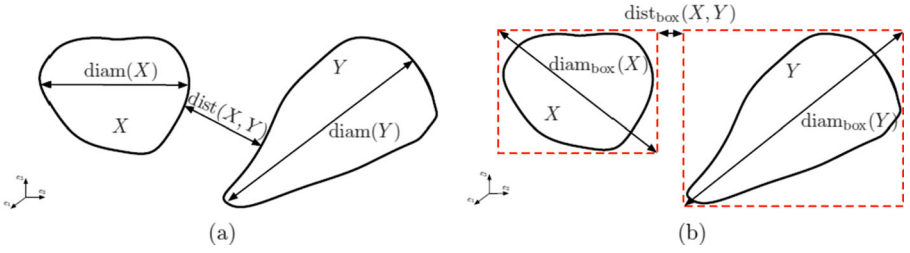

Fig. 4 Efficient implementation of the admissibility condition: (a) theoretical condition and (b) implemented condition

– ε_{decay}, which is the threshold parameter of the sparsification.

If we can define for a given wavenumber such an r_{lim}, we know that some blocks of the matrix will be full of zeros, or at least all their entries are sufficiently small so that the approximation can be chosen as a 0-rank approximation, i.e., it is also full of zeros. The aim of this section is thus to determine if we can complement the standard admissibility condition (6) to take into account these sparse blocks.

In the discussion below, the wavenumber is denoted by $k \in \mathbb{C}$ with $Im(k) > 0$. In the recent report [12], sparsification of oscillatory kernels with damping is also considered. One adjustable parameter is the order $\tilde{m}$ of the polynomials required to approximate the oscillatory kernel on a given admissible block $X \times Y$. Precisely in [12, definition (3.9)] the order of approximation $\tilde{m}$ is chosen so that the Chebyshev interpolation of the oscillatory kernel on the given admissible block $X \times Y$ achieves the requested approximation error. It is noted that if the resulting order is strictly lower than 0 ($\tilde{m} = -1$), then the entries are sufficiently small so that the approximation is made of zeros. In this particular case the approximation boils down to a 0-rank approximation. Interestingly, a rigorous mathematical analysis is carried out, and the order of approximation $\tilde{m}$ on the given admissible block $X \times Y$ is chosen so that (see [12, bottom of page 11]):

$$C_0 \, \rho_0^{-\tilde{m}} \left| \frac{\exp(i\sigma kr)}{r} \right| \leq \varepsilon_{error} \tag{8}$$

where $\varepsilon_{error} > 0$ is the target approximation error, while σ, $C_0 > 0$, and $\rho_0 > 1$ are given values (see again [12, §4]). So, up to some scaling factor, we note that condition (8) with $\tilde{m} = -1$ is completely similar to the proposed condition (7). Interestingly, even though empirical (7) is based on a sound mathematical analysis thanks to the equivalent condition (8) that is proposed and analyzed in [12]. Now, there remains to take into account those blocks that fulfil condition (7). We propose a heuristic condition, see (9) below. The major difference with [12] is that we do not limit the search to admissible blocks.

The first important remark concerns admissible blocks that fulfil condition (6) when an algebraic approach is used to perform the low-rank approximation (which is another difference with [12]). A priori, the numerical rank of a block full of zeros is 0, so the ACA will automatically perform a low-rank approximation with a rank equal to 0. And if all the admissible blocks are blocks full of zeros then the maximal numerical rank of admissible blocks r_{ACA}^{max} is equal to 0. Second, one has to check whether some additional gains can be obtained on the storage of the non-admissible blocks, when they are made of entries with small/negligible values. This is the main originality of our new admissibility condition. In relation with the definition (7) of r_{lim}, we add a condition based on the distance between clusters of non-admissible blocks. When $r_{ACA}^{max} = 0$, we propose the following simple admissibility condition to take into account potential non-admissible blocks full of zeros:

If $r_{ACA}^{max} = 0$, a non-admissible block $X \times Y$ is replaced by a matrix of zeros if $\text{dist}(X, Y) \geq r_{lim}$. (9)

The aim of the additional admissibility condition (9) is to further reduce storage requirements by approximating a large number of non-admissible blocks by matrices full of zeros. Note that it is tested only if all admissible blocks can already be approximated by matrices full of zeros, i.e., if $r_{ACA}^{max} = 0$. This is a conditional test that may, or may not, be implemented, in the limit of ε_{decay} tending to 0^+. Conditionality is expected to depend heavily on the damping.

Sparsification condition for oscillatory kernels For an oscillatory kernel, possibly with damping, a well-known issue is to take into account its behavior depending on the direction. In the literature, this corresponds to the so-called $\mathcal{H}^2$-matrix, or directional, methods. We refer again to [12, definition 3.2], where an admissibility condition is proposed in the context of directional $\mathcal{H}^2$-matrices for Helmholtz problems with complex frequencies. For a wavenumber $k \in \mathbb{C}$ with $Im(k) > 0$, and given $\boldsymbol{\eta} = (\eta_i)_{i=1}^3 \in \mathbb{R}^3_{>0}$, the admissibility condition writes: a pair of clusters $X, Y \in \mathcal{T}_I$ and a direction $c \in \mathbb{S}_2$ (unit sphere in $\mathbb{R}^3$) are said to be $\boldsymbol{\eta}$-admissible if they satisfy the following three conditions:

$$|Re(k)| \left\| \frac{M_X - M_Y}{\mathrm{dist}(M_X, M_Y)} - c \right\| \leqslant \frac{\eta_1}{\max\{\mathrm{diam}^2(X), \mathrm{diam}^2(Y)\}} \tag{10a}$$

$$\max\{\mathrm{diam}(X), \mathrm{diam}(Y)\} \leqslant \eta_2 \, \mathrm{dist}(X, Y) \tag{10b}$$

$$|Re(k)| \, \max\{\mathrm{diam}^2(X), \mathrm{diam}^2(Y)\} \leqslant \max\{\eta_2, \eta_3(Im(k))\mathrm{dist}(X, Y)\} \, \mathrm{dist}(X, Y) \tag{10c}$$

The first condition, i.e., (10a), corresponds to the choice of the sector in the directional approach, with M_X and M_Y respectively the centers of the clusters X and Y, while c is a unit vector defining the direction along which the wave is travelling. This is the purely directional condition, which is included in the choice of C_0 from condition (8) (see formula (4.5) from Lemma 4.1 page 15 in [12]).

Then, condition (10b) is similar to the standard admissibility condition (6). Furthermore, they are equivalent for clusters of similar size.

In this work we focus on the understanding of condition (10c) which is used to determine when a sparse approximation can be performed. (10c) is an adaptation of the $\mathcal{H}^2$ part of the admissibility condition for kernels with complex wavenumbers. Importantly, this condition reduces the set of admissible blocks compared to the standard admissible condition in $\mathcal{H}$-matrices. (10c) includes two criteria that we separate below, see (11) and (12). If $Im(k)$ is large enough (we will explain what it means in the following), the condition (10c) becomes:

$$|Re(k)| \max\{\mathrm{diam}^2(X), \mathrm{diam}^2(Y)\} \leqslant \eta_3(Im(k))\mathrm{dist}^2(X, Y) \tag{11}$$

This criterion becomes less and less restrictive as the value of damping ratio $\alpha = Im(k)/Re(k)$ increases, meaning that it does not significantly reduce the set of admissible blocks compared to standard $\mathcal{H}$-matrices. On the other hand, if $Im(k)$ is small (which includes the limiting case $Im(k) = 0$) then (10c) simplifies to the standard condition for $\mathcal{H}^2$-matrices in the case without damping [11]

$$|Re(k)| \max\{\mathrm{diam}^2(X), \mathrm{diam}^2(Y)\} \leqslant \eta_2 \mathrm{dist}(X, Y) \tag{12}$$

Finally, (10c) reduces to (10b) if $|Re(k)| \sim (\max\{\text{diam}(X), \text{diam}(Y)\})^{-1}$ and $Im(k)$ is small.

The previous considerations have been derived for the Helmholtz equation but can be extended straightforwardly to elastodynamics since, in that case, the Green's tensors are only linear combinations of derivatives of the Helmholtz Green's function. In elasticity, to avoid any ambiguity due to the coexistence of P and S waves, we choose to define the damping ratio as $\alpha_s = Im(k_s)/Re(k_s)$.

Figure 5 illustrates on an example ($\eta_2 = 2$, $\eta_3 = 0.5$, $Re(k_s) = 18$ and $Im(k_s) = 0.3$) how the two criteria (11) and (12) help realize condition (10c). We represent the different scenarios for various hypothetical distances $y = \text{dist}(X, Y)$ and diameters $x = \max(\text{diam}(X), \text{diam}(Y))$ of the blocks. The blue curve shows the limit when criterion (12) becomes satisfied and the red curve the limit when criterion (11) becomes satisfied. Obviously, there are four scenarios:

- both criteria hold;
- only criterion (11) holds;
- only criterion (12) holds;
- no criterion holds;

Let's now see how (10c) works in practice, for different damping ratios α_s. For all the remaining of this work, we define $\mathbb{G}$ as the $3N_c \times 3N_c$ matrix corresponding to the discretization of the 3D visco-elastodynamic Green's tensor at the N_c discretization points. This matrix is further decomposed into nine submatrices $(\mathbb{G}_{\alpha\beta})_{1\leq\alpha,\beta\leq3}$, each submatrix $\mathbb{G}_{\alpha\beta}$ corresponding to the discretization of the $G_{\alpha\beta}$-component of the Green's tensor. We consider a practical implementation on a sphere of radius $a = 1$,

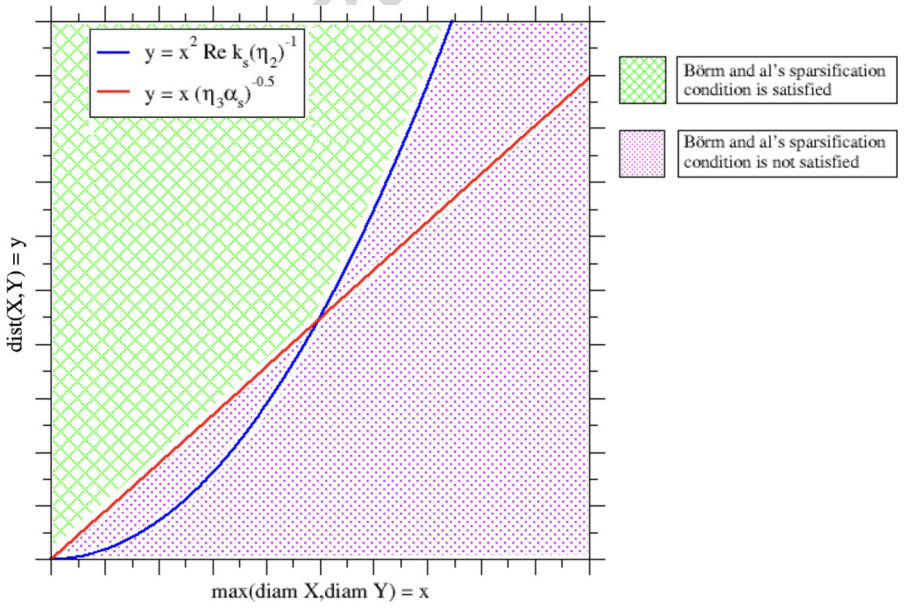

Fig. 5 Sparsification condition (10c): criterion (11) vs. criterion (12)

resulting in a 10274×10274 $\mathbb{G}_{11}$ matrix after discretization. All the different blocks of the $\mathcal{H}$-matrix representation are represented by black squares. The blocks are thus admissible if the square is located above the blue curve or the red curve. As a first illustration, see Fig. 6, we consider $N_{\text{leaf}} = 100$ and four values of damping ratio: $\alpha_s = 0.01$, 0.1, 1 and 100. The wavenumber is chosen to yield a fixed density of points of 10 points per wavelength, i.e., $k_s a = 18$. We see that for a small damping ratio ($\alpha_s = 0.01$ and 0.1), the condition (10c) is not satisfied at all. For a larger damping ratio $\alpha_s = 1$, some blocks satisfy (11) but none of them satisfies (12). In that case, (10c) is equivalent to (11). Even if a greater number of blocks are admissible with respect to criterion (11) for $\alpha_s = 100$, criterion (12) is never fulfilled. In this setting, we conclude that condition (10c) is not satisfied when the damping ratio remains *small*. And, when the damping ratio increases, it seems that (11) is the dominant criterion to realize condition (10c). These results are in agreement with our expectation of a restrictive criterion for small damping ratios.

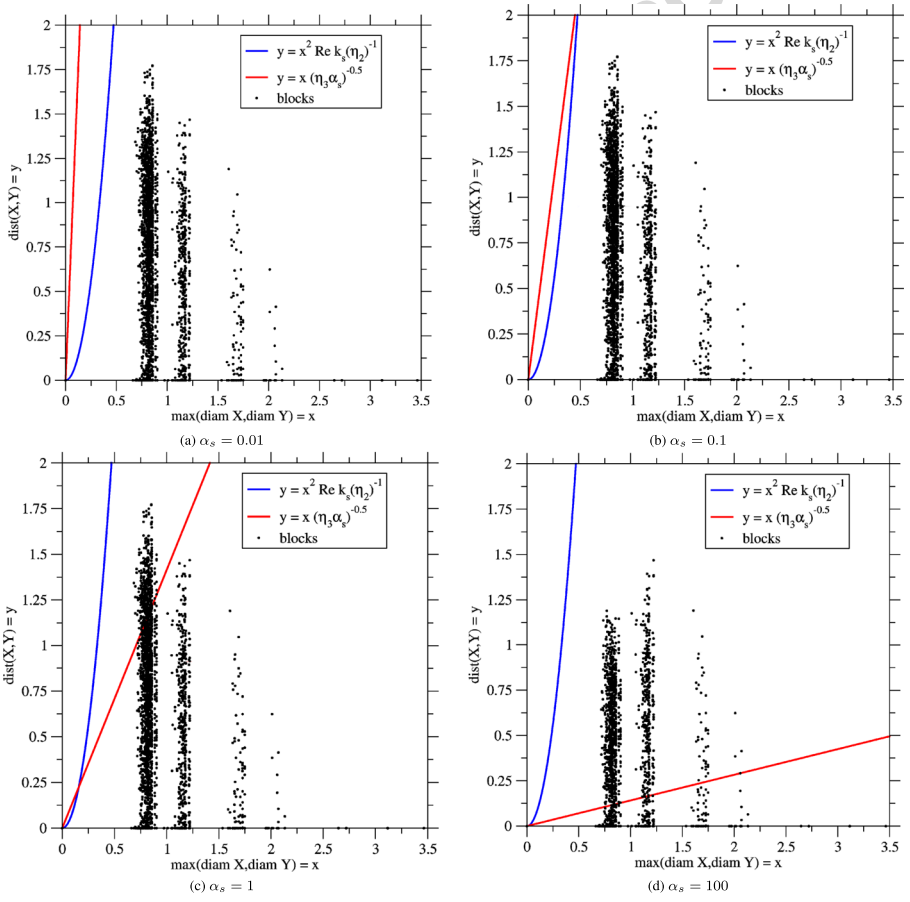

Fig. 6 Sparsification condition (10c): criterion (11) vs. criterion (12) for different damping ratios [$N_{\text{leaf}} = 100$; $Re(k_s)a = 18$]

On the other hand, the fact that condition (10c) holds through (11) or (12) depends on the stopping criterion N_{leaf} used in the binary tree. Indeed, we observe that if the value of N_{leaf} is decreased, then one gets smaller clusters, i.e., with a smaller diameter. So, we consider the same geometry, now with $N_{\text{leaf}} = 20$. Figure 7 shows that for a small damping ratio $\alpha_s = 0.01$, some blocks satisfy (12) but that none of them satisfies (11), so (10c) is equivalent to (12). For $\alpha_s = 0.1$ some blocks satisfy both (12) and (11) criteria but (12) has become the dominant criterion. Then for $\alpha_s = 1$, some blocks satisfy both (12) and (11) criteria, and (11) is the dominant criterion. Finally for $\alpha_s = 100$, a majority of blocks satisfy (11) and there is a very small number of blocks which satisfy (12): (11) is the dominant criterion again. So, it appears that when N_{leaf} is small, in the sense that a wider distribution of diameters towards 0 is at hand, the different scenarios expected in Fig. 5 can actually be observed: condition (10c) is met even for a small damping ratio, and moreover either (11) or (12) is the dominant criterion.

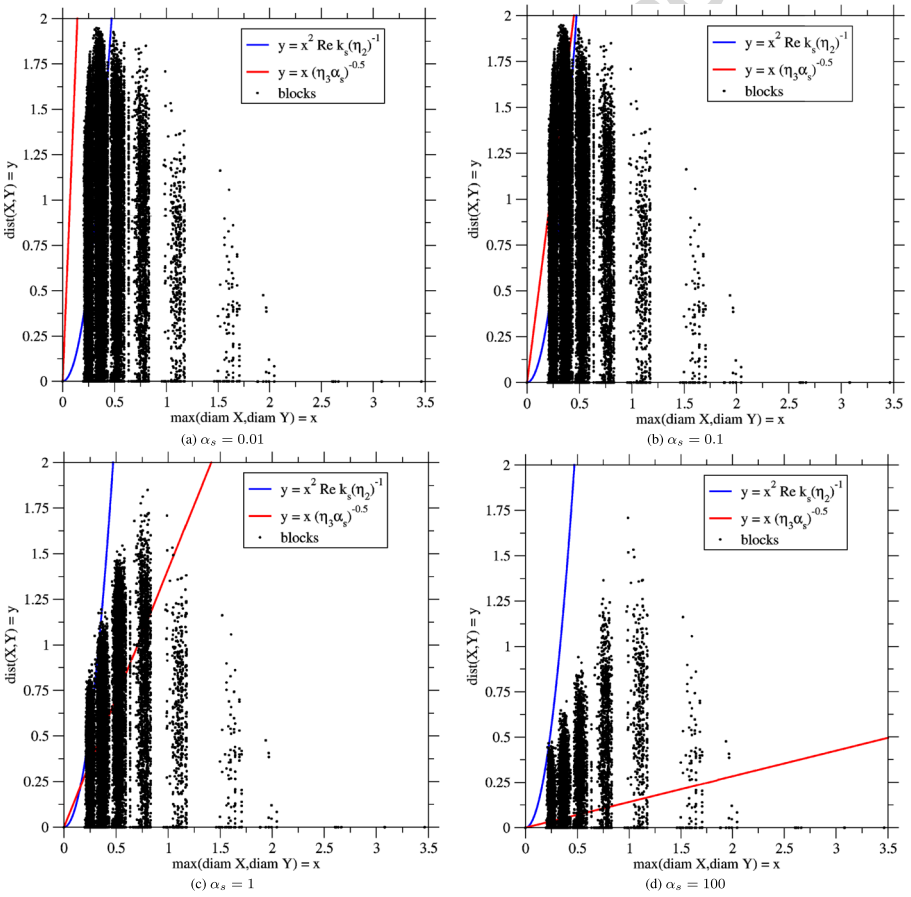

Fig. 7 Sparsification condition (10c): criterion (11) vs. criterion (12) for different damping ratios [$N_{\text{leaf}} = 20$; $Re(k_s)a = 18$]

It is also possible to get the same kind of results by decreasing the frequency in order to change the referenced position of both the blue curve and the red curve. Figure 8 presents the same results but when the frequency is divided by 10, leading to about 100 points per wavelength. For the small damping levels $\alpha_s = 0.01$ and $\alpha_s = 0.1$, some blocks satisfy (12) but none of the blocks satisfies (11), so condition (10c) is equivalent to (12). For $\alpha = 1$, some blocks satisfy (12) and (11), but the majority of blocks satisfy (12); thus, (10c) is equivalent to (12). Finally for $\alpha_s = 100$, some blocks satisfy (12) and (11), but the majority of blocks satisfy (11); thus, (10c) is equivalent to (11). As a conclusion, it appears from these tests that decreasing (respectively increasing) the frequency, and as a consequence the value of $Re(k_s)$, leads to a wider (respectively tighter) parabola and to swap the dominant condition between (11) and (12).

At this point, it is important to sum up our understanding on $\mathcal{H}$-matrices for oscillatory kernels with a complex wavenumber. To our best knowledge, the only work on the subject in the literature is [12]. But this work is dedicated to the

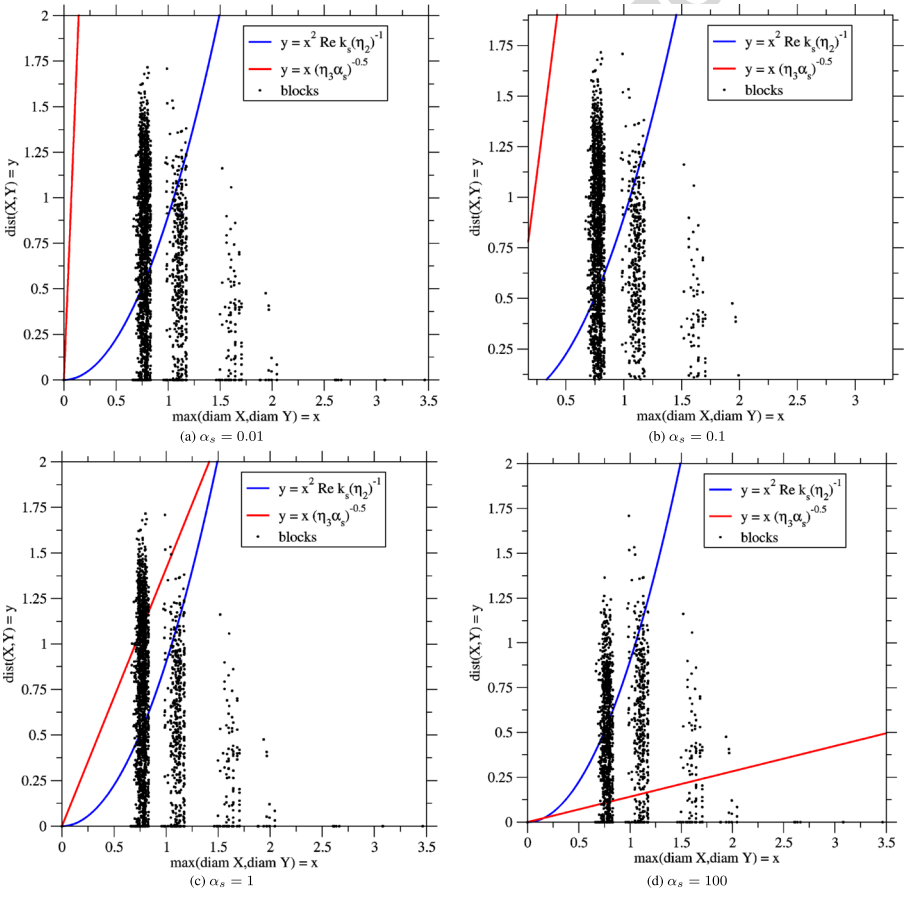

Fig. 8 Sparsification condition (10c): criterion (11) vs. criterion (12) for different damping ratios [$N_{\text{leaf}} = 100$, $Re(k_s)a = 1.80$]

improvement of directional $\mathcal{H}^2$-matrices for oscillatory kernels with a complex wavenumber. The tests we have performed show that the proposed improvement is in fact to relax the third condition in this admissibility condition (the one that is specific to $\mathcal{H}^2$-matrices) according to the level of damping in the kernel. However, it appears that this adaptation can still be improved on two aspects since:

- its only aim is to relax the $\mathcal{H}^2$ part of the admissibility condition; In some sense it increases the number of admissible blocks; However it remains more restrictive than standard $\mathcal{H}$-matrices.
- it does not test non-admissible blocks to take advantage of the introduction of the complex wavenumber and thus one can not obtain further gain by compressing some of those blocks.

In the next section, we perform extensive numerical tests to check if our new admissible condition enables to take these aspects into account and achieve better compression efficiency than $\mathcal{H}^2$-matrices.

4 Efficiency of the new admissibility condition for standard $\mathcal{H}$-matrices

In this section, numerical experiments are conducted to compare both admissibility conditions ((6)+(9)) and their "counterpart" ((10b)+(10c)). To that aim, we study a wave propagation problem in a visco-elastic media containing an obstacle represented by a sphere of radius $a = 1$.

4.1 Practical parameters for the sparsification condition from [12]

The additional condition (8) where $\tilde{m} = -1$ enables to replace the admissible blocks by matrices of zeros in the approximated Green's tensor. By definition of r_{min}, we know that $r \geq r_{min}$ in (8). In the following we assume that $0 < \varepsilon_{error} \leq r_{min}$. By applying the log on both sides of the inequality and "neglecting the constant," i.e., setting $C_0\rho_0$ to 1, we obtain the *sufficient condition*:

$$\log\left(\frac{1}{\varepsilon_{error}}\right)\frac{2}{\sigma r} \leq Im(k) \tag{13}$$

By sufficient we mean that:

- condition (8) and condition (13) are equivalent if $\varepsilon_{error} \sim r$;
- condition (13) implies condition (8) if $\varepsilon_{error} \ll r$.

We now choose the value of σ to implement the condition (13) for our practical applications. To do that, we apply the condition (13) with $k = k_s$ and $\varepsilon_{error} = r_{min}$, in conjunction with the admissibility condition (10). The number of discretization points is $N_c = 10274$ ($\varepsilon_{error} = 0.0253$), and a frequency corresponding to $Re(k_s)a = 18$ (in order to have roughly 10 points per wavelength). For a damping ratio $\alpha_s = 100$, one finds by direct inspection that $r_{ACA}^{max} = 0$ (and then all admissible blocks can be replaced by matrices of zeros). Testing the condition (13) in the

submatrix $\mathbb{G}_{11}$ for different values of σ among $\{10^{-4}, 10^{-3}, \ldots, 0.5, 1, 2, \ldots, 10^4\}$, we find that it is satisfied for all admissible blocks and for all values of σ, except 10^4. So, in the rest of the manuscript, we will keep the above condition with $\sigma = 2$, which simplifies to

$$\log\left(\frac{1}{\varepsilon_{error}}\right)\frac{1}{r} \leq Im(k) \tag{14}$$

as a practical implementation of the additional condition (8).

4.2 Practical choices and illustration of the new admissibility condition

The parameters used in all this section are given in Table 1. ω is chosen again to achieve about 10 points per wavelength λ_s.

The first parameter is r_{lim} that appears in the condition (9). For a fixed value ε_{decay} in condition (7), we are able to determine r_{lim} by observing the evolution of $\frac{\exp(-Im(k_p)r)/r}{\exp(-Im(k_p)r_{min})/r_{min}}$ with respect to r for different values of k_p. Indeed, comparing condition (7) with $k = k_p$ and $k = k_s$, we observe that it is more restrictive with k_p than with k_s, because $0 < Im(k_p) < Im(k_s)$. We first conduct a numerical experiment to determine the influence on the overall accuracy of the tolerance ε_{decay} in (7). We perform the analysis with the conditions ((6)+(9)) and

$$\alpha_s = Im(k_s)/Re(k_s) \in \{11, 20, 33, 66, 100, 500, 1000, 10000\}$$

Let $\mathbb{G}_{app}$ be the approximated version of $\mathbb{G}$. As a matter of fact, as soon as condition (9) is fulfilled we only introduce error due to the approximated non-admissible blocks (i.e., only those blocks that meet condition (9)) since admissible blocks are equal to zero and do not contribute to the Frobenius norm, we consider the relative error:

$$err_{rel} = \left(\frac{||\mathbb{G}_{11} - (\mathbb{G}_{11})_{app}||_F}{||\mathbb{G}_{11}||_F}\right)_{\text{among non-admissible blocks}} \tag{15}$$

This relative error might be too strict compared to the error observed in a BEM solver. It represents the upper bound of the error obtained for example when a matrix-vector product is performed in the iterative solver. However in practice, it is quite close to the achieved bound. This error can be easily linked to the error performed in the case we want to solve a system such that the ones encountered in the context of the BEM. If we consider the system $\mathbb{G}_{11_{app}}\mathbf{X}_{app} = \mathbf{b}$ instead of $\mathbb{G}_{11}\mathbf{X} = \mathbf{b}$, then the error introduced on the solution is bounded by (e.g., [15, Theorem 2.2-1 p49 and Theorem 1.4-4 p28])

$$\frac{||\mathbf{X} - \mathbf{X}_{app}||_2}{||\mathbf{X}_{app}||_2} \leq \text{cond}_F(\mathbb{G}_{11})err_{rel}$$

In Table 2 we report these errors for three values of ε_{decay} together with the number of non-admissible blocks approximated by a block full of zeros. Importantly for this example, with the parameters used, we have a total of 2 242 blocks, 828 of them being non-admissible with the standard admissibility condition. We note that as expected, this additional approximation has an effect on the accuracy of the data-sparse approximation. However for $\varepsilon_{decay} = 10^{-10}$, the relative error on the Green's tensor is always well below 10^{-3}. In comparison, the relative approximation errors

Table 1 Parameters

Parameter type	Material characteristics			S and P waves			Discretization	H-matrices			
Admissibility condition	μ	λ	ν	$\alpha_s = Im(k_s)/Re(k_s)$	$Re(k_p)$	$Re(k_s)a$	N_c	N_{leaf}	η		ε_{ACA}
((6)+(9))	1	2	$\frac{1}{3}$	{0, 0.01, 0.1, 1, 10, 100, 1000, 10000}	$k_s/2$	18	10274	100	$\eta = 3$		10^{-4}
(10)	1	2	$\frac{1}{3}$	{0, 0.01, 0.1, 1, 10, 100, 1000, 10000}	$k_s/2$	18	10274	100	$\eta_1 = 10$	$\eta_2 = 2$ $\eta_3 = 1/2$	10^{-4}

Table 2 Evolution of err_{rel_1} with respect to the damping ratio and tolerance in condition (7) [$Re(k_s)a = 18$]

Damping ratio	$err_{rel}\ \varepsilon_{decay} = 10^{-3}$	Blocks (9) $\varepsilon_{decay} = 10^{-3}$	$err_{rel}\ \varepsilon_{decay} = 10^{-5}$	Blocks (9) $\varepsilon_{decay} = 10^{-5}$	$err_{rel}\ \varepsilon_{decay} = 10^{-10}$	Blocks (9) $\varepsilon_{decay} = 10^{-10}$
11	$2.49\ 10^{-2}$	406	$1.66\ 10^{-4}$	330	$4.25\ 10^{-10}$	174
20	$2.16\ 10^{-2}$	414	$1.41\ 10^{-2}$	374	$1.48\ 10^{-9}$	252
33	$1.04\ 10^{-2}$	418	$9.10\ 10^{-3}$	404	$1.62\ 10^{-7}$	312
66	$1.72\ 10^{-3}$	424	$1.55\ 10^{-3}$	414	$6.09\ 10^{-4}$	390
100	$3.50\ 10^{-4}$	430	$3.45\ 10^{-4}$	420	$3.41\ 10^{-4}$	406
500	$2.29\ 10^{-10}$	438	$6.23\ 10^{-13}$	436	$9.36\ 10^{-14}$	426
1000	$< 10^{-16}$	442	$< 10^{-16}$	438	$< 10^{-16}$	434
10000	$< 10^{-16}$	444	$< 10^{-16}$	444	$< 10^{-16}$	444

reach a maximum of about 1.5 10^{-2} for a tolerance $\varepsilon_{decay} = 10^{-5}$ and about 3 10^{-2} for a tolerance $\varepsilon_{decay} = 10^{-3}$. We performed the same tests on larger problems with N_c roughly equal to respectively 30 000, 60 000 and 100 000. In these cases, the error follow the same trends. These results seem to advocate in favor of the use of $\varepsilon_{decay} = 10^{-10}$. The key point is that, depending on the accuracy needed for a given configuration, this parameter can be tuned. The accuracy of the low-rank approximation is not the only factor to take into account. This criterion has also an influence on the number of blocks which can be replaced by matrices full of zeros and thus on the data compression rate. From Table 2, we anticipate more savings while the damping ratio increases. We will consider this aspect next.

Now that we have an insight on the effect of ε_{decay} on the accuracy, Fig. 9 illustrates the behavior of the dominant factor in the elastodynamic Green's tensor (if a complex wavenumber is considered). This figure shows in particular that, as expected, if the damping ratio increases the required value of r_{lim} decreases.

We now compare the effect of the additional condition (9) to complement the classic admissibility condition (6) on the submatrix $\mathbb{G}_{11}$. On Fig. 10a, admissible (and zero) blocks are in blue and red blocks represent non-admissible blocks. In comparison, Fig. 10b show the distribution if only condition (6) is enforced. A significant gain of storage is clearly visible as the number of red blocks is quite smaller in Fig. 10b than in Fig. 10a. The observed data compression rates are $\tau = 0.104$ with the conditions ((6)+(9)) to be compared to $\tau = 0.202$ with the standard condition (6).

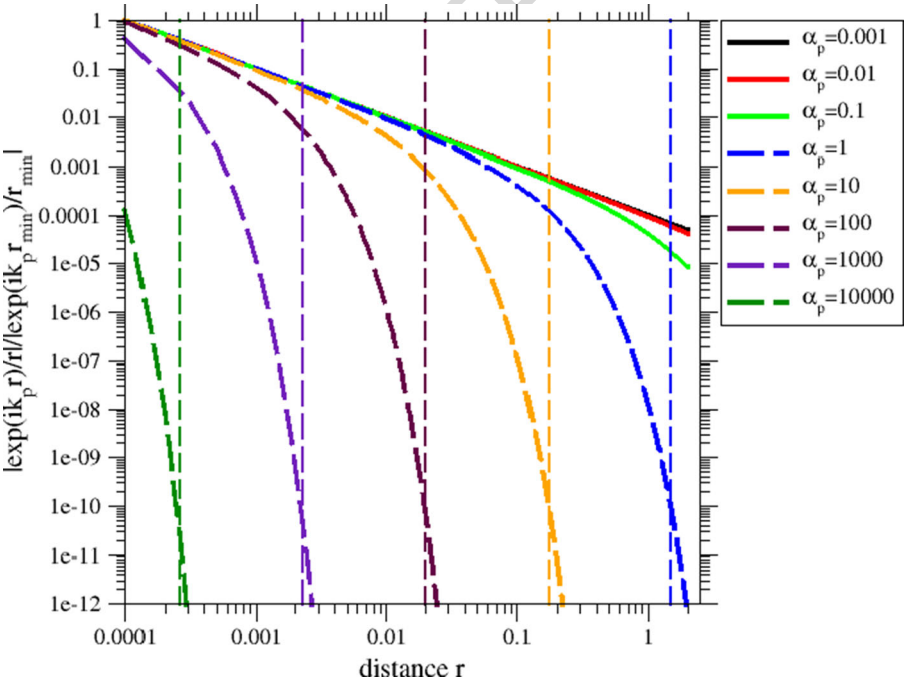

Fig. 9 Evolution of the dominant factor in the elastodynamic (with a complex wavenumber) Green's tensor with respect to the distance for tolerance $\varepsilon_{decay} = 10^{-10}$ and different damping ratios $[Re(k_p)a = Re(k_s)a/2 = 9]$

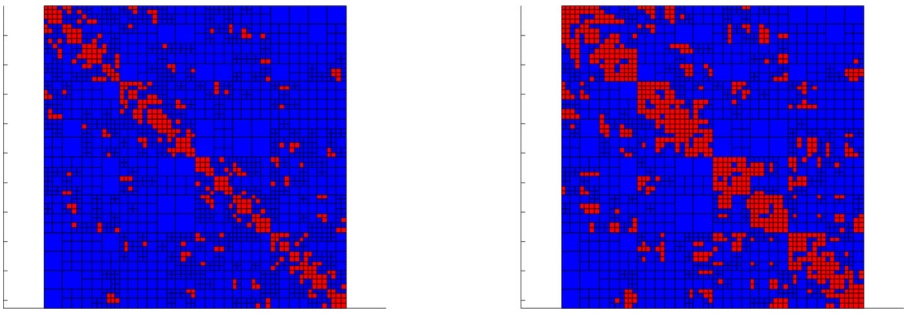

(a) Improved condition - $\tau = 0.104$ (b) Standard condition - $\tau = 0.202$

Fig. 10 Illustration with colored patches of the type of blocks represented when (a) conditions ((6)+(9)) are enforced and (b) when only (6) is applied with a damping ratio $\alpha_s = 100$; tolerance is set to $\varepsilon_{decay} = 10^{-10}$ $[Re(k_s)a = 18]$

We illustrate in Fig. 11 three different tolerances ε_{decay} for $\alpha_s = 15$ to show that the difference in the storage is not very significant. In Table 3 we gather the data compression rates for different tolerances ε_{decay} and damping ratios α_s. Note that in

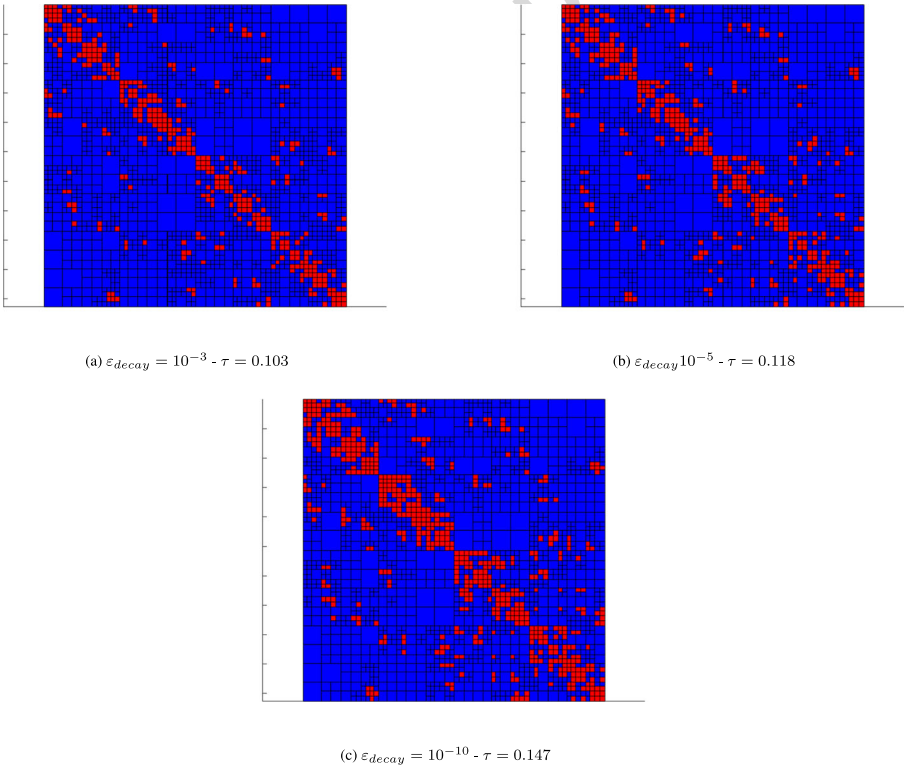

(a) $\varepsilon_{decay} = 10^{-3}$ - $\tau = 0.103$ (b) $\varepsilon_{decay} 10^{-5}$ - $\tau = 0.118$

(c) $\varepsilon_{decay} = 10^{-10}$ - $\tau = 0.147$

Fig. 11 Illustration with colored patches of the type of blocks represented when conditions ((6)+(9)) are applied for a damping ratio $\alpha_s = 15$ and different tolerances ε_{decay} $[Re(k_s)a = 18]$

Table 3 Evolution of the data compression rate τ (expressed in thousandths for more readability) with respect to the damping ratio and to the tolerance in condition (7) [$Re(k_s)a = 18$]

Damping ratio α_s	τ with (6) only	τ with (6) + (9) $\varepsilon_{decay} = 10^{-3}$	τ with (6) + (9) $\varepsilon_{decay} = 10^{-5}$	τ with (6) + (9) $\varepsilon_{decay} = 10^{-10}$
0	317	317	317	317
0.01	317	317	317	317
0.1	315	315	315	315
1	292	292	292	292
10	202	202	202	202
15	202	103	118	147
100	202	99.9	101	104
1000	202	95.4	96.5	97.5
10000	202	94.9	94.9	94.9

all the following tables (Tables 3, 4, 5, 6, 7, and 8), compression rates are given in thousandths for more readability. In practice, the tolerance has a very moderate influence on the data compression rate in this exhaustive comparison. Moreover, the best result is almost always achieved with its smallest value. Based on these observations, we set $\varepsilon_{decay} = 10^{-10}$ in the following.

4.3 Influence of the condition (10c)

Now that all the practical choices have been made for the parameters, numerical experiments are conducted to compare both admissibility conditions ((6)+(9)) and their more involved "counterpart" ((10b)+(10c)). The present objective is to investigate whether the additional admissibility condition (9) leads to better, or worse, data compression, compared to the conditions ((10b)+(10c)) and $(14)_{k=k_s}$.

Table 4 Evolution of the data compression rate τ (expressed in thousandths for more readability) with respect to the damping ratio and parameter η_2 [$Re(k_s)a = 18$]

Damping ratio α_s	τ with (6) only	τ with (6) + (9) $\varepsilon_{decay} = 10^{-10}$	τ with (10b) + (10c) + (14) η_2=2	τ with (10b) + (10c) + (14) η_2=3
0	317	317	1000	1000
0.01	317	317	1000	1000
0.1	315	315	1000	1000
1	292	292	799	799
10	202	202	278	254
15	202	147	278	222
100	202	104	278	209
1000	202	97.5	278	209
10000	202	94.9	278	209

Table 5 Evolution of the compression rate τ (expressed in thousandths for more readability) with respect to the damping ratio for different admissibility conditions [$Re(k_s)a = \{18, 18 \times 5\}$ with 10 points per λ_s, $N_{leaf} = 100$]

Damping ratio α_s	τ: $Re(k_s) = 18$ (6) only	τ: $Re(k_s) = 18$ (6) + (9) $\varepsilon_{decay} = 10^{-10}$	τ: $Re(k_s) = 18$ (10b) + (10c) + (14) η_2=2	τ: $Re(k_s) = 18$ (10b) + (10c) + (14) η_2=3	τ: $Re(k_s) = 90$ (6) only	τ: $Re(k_s) = 90$ (6) + (9) $\varepsilon_{decay} = 10^{-10}$	τ: $Re(k_s) = 90$ (10b) + (10c) + (14) η_2=2	τ: $Re(k_s) = 90$ (10b) + (10c) + (14) η_2=3
0	317	317	1000	1000	33.2	33.2	404	250
0.03	317	317	1000	1000	32.5	32.5	310	160
0.04	317	317	1000	1000	32.0	32.0	291	160
0.05	317	317	1000	1000	31.4	31.4	267	160
0.06	316	316	1000	1000	30.7	30.7	235	157

Table 6 Number of complex frequencies lying in some damping ratio intervals for BDF2 and BDF3 integration contours

Intervals of α_s	Number of complex frequencies for BDF2 integration contour Fig. 15a	Number of complex frequencies for BDF3 integration contour Fig. 15b
[0,1]	6850	6580
[1,10]	8080	10702
[10,30]	1830	1826
[30,60]	898	448
[60,100]	646	178
[100,600]	1696	222
[600,17000]	0	44

The parameters used in this section are gathered in Table 1. We use $\eta_2 = 2$ as it is the optimal choice proposed in [10] and $\eta = 3$ as it is the optimal choice of η resulting from the analysis detailed in [14].

First we consider the conditions ((6)+(9)). Figure 12 illustrates the evolution of the data-sparse approximation (and gives the corresponding data compression rate τ) for different values of the damping ratio α_s. We observe as expected that the compression improves with the increase of the damping ratio. This is explained by the decrease of the value of r_{lim}, cf. condition (7) (see Fig. 9).

Now we consider the same configuration but use the more involved criterion ((10b)+(10c)+(14)). Figure 13 shows the results for $\eta_2 = 2$, while Fig. 14 shows the results for $\eta_2 = 3$. This latter case (see (10b)) is similar to the application of the classical admissibility condition (6). It allows us to see more precisely the influence of (10c)+(14). By comparing Figs. 10b and 14b, it seems that $\eta_2 = 3$ enables to have similar results between (6) and ((10b)+(10c)+(14)). To confirm these results, Table 4 gives the data compression rates for various admissibility conditions and damping ratio α_s. It appears that the condition ((10b)+(10c)+(14)) does not give results better than the ones obtained with (6).

To conclude, and based on all the previous numerical studies, it appears that the use of (9) in addition to the classical condition (6) enables important storage reductions compared to the other approaches. These encouraging results on the efficiency of standard $\mathcal{H}$-matrices can be easily explained. Comparing the involved $\mathcal{H}^2$ ((10b)+(10c)+(14)) condition with the improved, yet simple $\mathcal{H}$ ((6)+(9)) condition, we emphasize two important aspects:

– The set of admissible blocks in the $\mathcal{H}^2$ case is, by definition, a subset of the set of admissible blocks in the $\mathcal{H}$ case. This restriction is based on an a priori study, specifically designed to exclude blocks which are not low-rank. However, it appears in the case with a complex wavenumber that the standard $\mathcal{H}$ condition is already efficient and does not need to be restricted. Otherwise it leads to a less efficient approach.

JmlID 10444_ArtID 09921_Proof#1 - 16/01/2022

Table 7 Evolution of the compression rate τ (expressed in thousandths for more readability) with respect to reachable damping ratios in BDF2 integration's contour Fig. 15a for different admissibility conditions [$Re(k_s)a = \{18, 90\}$, with 10 points per λ_s, $N_{leaf} = 100$]

Damping ratio α_s	τ with $Re(k_s) =$ 18 (6) only	τ with $Re(k_s) =$ 18 (6) + (9) $\varepsilon_{decay} = 10^{-10}$	τ with $Re(k_s) =$ 18 (10b) + (10c) η_2=2	τ with $Re(k_s) =$ 18 (10b) + (10c) η_2=3	τ with $Re(k_s) =$ 90 (6) only	τ with $Re(k_s) =$ 90 (6) + (9) $\varepsilon_{decay} = 10^{-10}$	τ with $Re(k_s) =$ 90 (10b) + (10c) η_2=2	τ with $Re(k_s) =$ 90 (10b) + (10c) η_2=3
0	317	317	345	345	33.2	33.2	404	250
5	205	205	278	254	6.57	6.57	11.0	11.0
10	202	202	278	209	6.17	6.17	8.67	7.87
20	202	141	278	209	6.16	4.73	8.67	6.44
30	202	130	278	209	6.16	4.44	8.67	6.44
40	202	119	278	209	6.16	4.22	8.67	6.44
50	202	117	278	209	6.16	4.07	8.67	6.44
100	202	104	278	209	6.16	3.54	8.67	6.44
130	202	103	278	209	6.16	3.42	8.67	6.44
160	202	103	278	209	6.16	3.33	8.67	6.44
200	202	102	278	209	6.16	3.25	8.67	6.44
215	202	102	278	209	6.16	3.22	8.67	6.44

JmlID 10444_ArtID 09921_Proof#1 - 16/01/2022

Table 8 Evolution of the compression rate τ (expressed in thousandths for more readability) with respect to reachable damping ratios in BDF3 integration's contour Fig. 15b for different admissibility conditions [$Re(k_s)a = \{18, 90\}$ with 10 points per λ_s $N_{leaf} = 100$]

Damping ratio α_s	τ with $Re(k_s) =$ 18 (6) only	τ with $Re(k_s) =$ 18 (6) + (9) $\varepsilon_{decay} = 10^{-10}$	τ with $Re(k_s) =$ 18 (10b) + (10c) η_2=2	τ with $Re(k_s) =$ 18 (10b) + (10c) η_2=3	τ with $Re(k_s) =$ 90 (6) only	τ with $Re(k_s) =$ 90 (6) + (9) $\varepsilon_{decay} = 10^{-10}$	τ with $Re(k_s) =$ 90 (10b) + (10c) η_2=2	τ with $Re(k_s) =$ 90 (10b) + (10c) η_2=3
0	317	317	345	345	33.2	33.2	404	250
5	205	205	278	254	6.57	6.57	11.0	11.0
10	202	202	278	209	6.17	6.17	8.67	7.87
20	202	141	278	209	6.16	4.73	8.67	6.44
30	202	130	278	209	6.16	4.44	8.67	6.44
40	202	119	278	209	6.16	4.22	8.67	6.44
50	202	117	278	209	6.16	4.07	8.67	6.44
100	202	104	278	209	6.16	3.54	8.67	6.44
130	202	103	278	209	6.16	3.42	8.67	6.44
160	202	103	278	209	6.16	3.33	8.67	6.44
200	202	102	278	209	6.16	3.25	8.67	6.44
500	202	99.5	278	209	6.16	3.06	8.67	6.44
1000	202	97.5	278	209	6.16	2.92	8.67	6.44
10000	202	94.9	278	209	6.16	2.78	8.67	6.44
16240	202	94.9	278	209	6.16	2.78	8.67	6.44

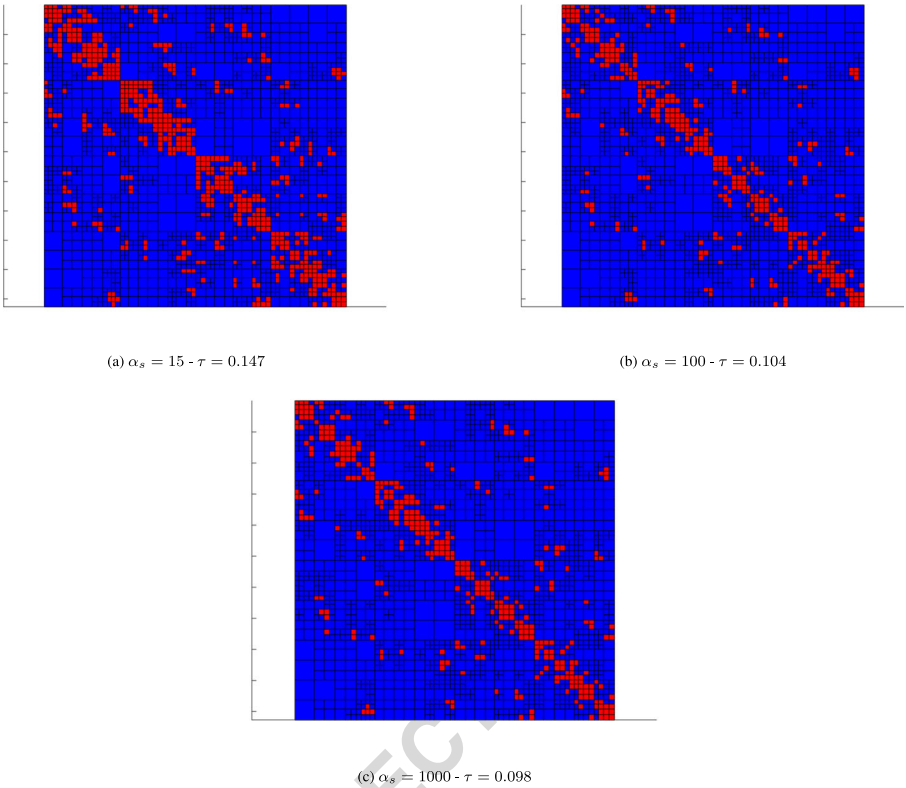

(a) $\alpha_s = 15$ - $\tau = 0.147$

(b) $\alpha_s = 100$ - $\tau = 0.104$

(c) $\alpha_s = 1000$ - $\tau = 0.098$

Fig. 12 Illustration with colored patches of the type of blocks represented when conditions (6+9) are applied for $\varepsilon_{decay} = 10^{-10}$, with different damping ratios α_s $[Re(k_s)a = 18]$

– The proposed improved $\mathcal{H}$ condition further reduces the storage requirements by approximating by blocks full of zero not only the admissible blocks but also a portion of non-admissible blocks (in the traditional sense of admissibility).

Due to its high efficiency and ease of implementation we advocate the use of standard "improved" $\mathcal{H}$-matrices for problems with an oscillatory kernel and a complex wavenumber. In the next section, we illustrate the practical efficiency of the proposed approach for two possible configurations: visco-elastodynamic problems in the frequency domain and purely elastic problems in the time domain.

5 Application in two configurations: visco-elastodynamic BEMs and Z-BEMs

5.1 Efficiency in the context of visco-elastodynamic BEMs

We consider first the case with a physical attenuation. We can write the constitutive equation for visco-elasticity as the convolution product of the relaxation tensor and

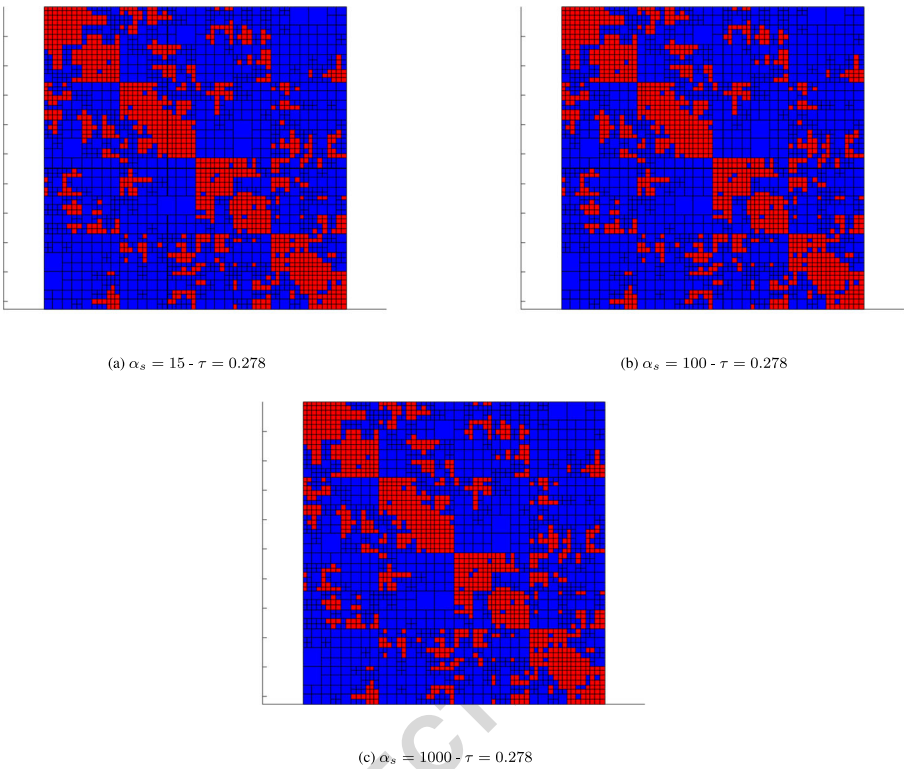

(a) $\alpha_s = 15$ - $\tau = 0.278$

(b) $\alpha_s = 100$ - $\tau = 0.278$

(c) $\alpha_s = 1000$ - $\tau = 0.278$

Fig. 13 Illustration with colored patches of the type of blocks represented when conditions (10b) and (10c) are applied with $\eta_2 = 2$ for different damping ratios α_s $[Re(k_s)a = 18]$

the strain rate:

$$\boldsymbol{\sigma}(\mathbf{x}, t) = \mathbf{C}(t) * \dot{\varepsilon}(\mathbf{x}, t) = \dot{\mathbf{C}}(t) * \varepsilon(\mathbf{x}, t) \tag{16}$$

For a homogeneous isotropic visco-elastic medium, the relaxation tensor $C_{ijkl}(t)$ is written in terms of two independent Lamé-type coefficients:

$$C_{ijkl}(t) = \left[\lambda(t)\delta_{ij}\delta_{kl} + \mu(t)(\delta_{ik}\delta_{jl} + \delta_{il}\delta_{jk})\right] H(t) \tag{17}$$

where $H(.)$ is a Heaviside step function. The rewriting of the visco-elastic constitutive law in the frequency domain, see [18] for more details, leads to:

$$\sigma_{ij}(\mathbf{x}, \omega) = \hat{C}_{ijkl}(\omega)\varepsilon_{kl}(\mathbf{x}, \omega), \quad \hat{C}_{ijkl}(\omega) = \hat{\lambda}(\omega)\delta_{ij}\delta_{kl} + \hat{\mu}(\omega)(\delta_{ik}\delta_{jl} + \delta_{il}\delta_{jk}) \tag{18}$$

where $\hat{\lambda}(\omega)$ and $\hat{\mu}(\omega)$ are respectively the Fourier transforms of $\lambda(t)H(t)$ and $\mu(t)H(t)$. This highlights the analogy between the linear visco-elastic and the linear elastic time-harmonic configurations. Equality (18) shows that the main difference between the two situations is that the Lamé coefficients and consequently wave velocities and wavenumbers are complex-valued and frequency-dependent in the

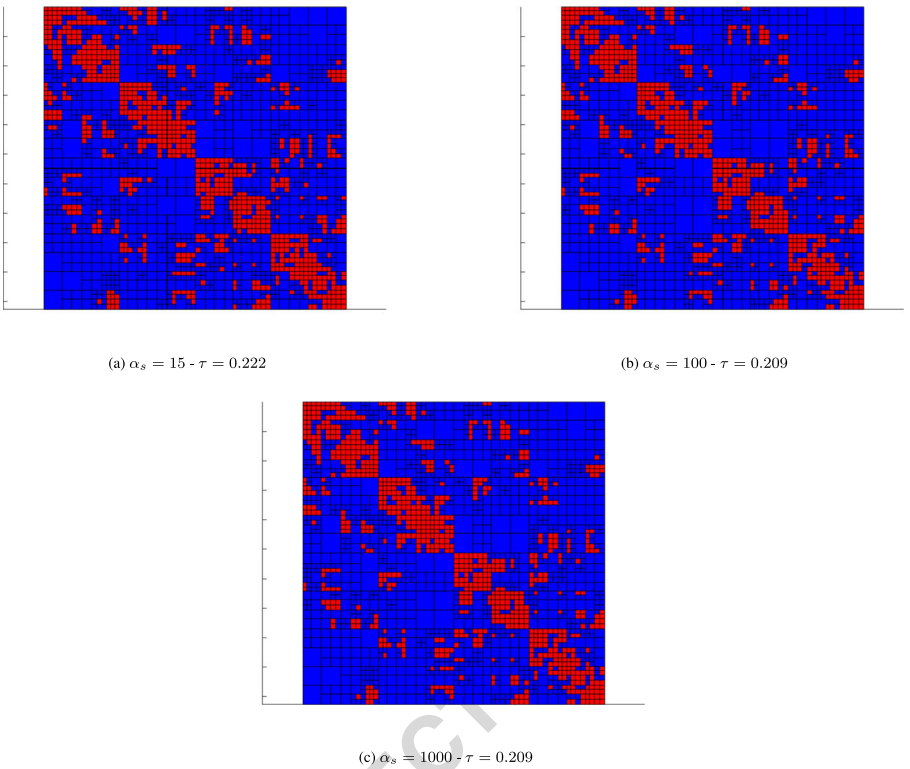

(a) $\alpha_s = 15$ - $\tau = 0.222$

(b) $\alpha_s = 100$ - $\tau = 0.209$

(c) $\alpha_s = 1000$ - $\tau = 0.209$

Fig. 14 Illustration with colored patches of the type of blocks represented when conditions (10b) and (10c) are applied with $\eta_2 = 3$ for different damping ratios [$Re(k_s)a = 18$]

visco-elastic case. Following [19], we consider complex wavenumbers of the form:

$$\hat{k}^2(\omega) = \frac{\rho\omega^2}{\hat{M}} \tag{19}$$

where $\hat{M}(\omega) = M_r(\omega) - iM_i(\omega)$, with $M_r > 0$ and $M_i \geq 0$, corresponds either to $\hat{M} = \hat{\lambda}$ or $\hat{\mu}$. These complex wavenumbers can be written as:

$$\begin{aligned}\hat{k}(\omega) &= \omega\sqrt{\frac{\rho(|\hat{M}| + M_r)}{2|\hat{M}|^2}} + i\omega\sqrt{\frac{\rho(|\hat{M}| - M_r)}{2|\hat{M}|^2}} \\ &= \omega\sqrt{\frac{\rho(|\hat{M}| + M_r)}{2|\hat{M}|^2}}\left(1 + i\sqrt{\frac{|\hat{M}| - M_r}{|\hat{M}| + M_r}}\right) = Re(\hat{k}(\omega))(1 + i\alpha(\omega))\end{aligned}$$

$\alpha(\omega)$ corresponds to the ratio of the imaginary part over the real part of the complex wavenumber for physical configuration in case of real soils. We denote Q^{-1} the damping coefficient associated with the physical material attenuation given by

$$Q^{-1} = \frac{M_i(\omega)}{M_r(\omega)} \tag{20}$$

It can be defined through empirical models, e.g., rheological models (Maxwell, Kelvin-Voigt, Zener) which are able to give the frequency-depend expression of the equivalent visco-elastic modulus (see [36] for more details on rheological models). Rewriting the expression of the attenuation factor $\alpha(\omega)$ as a function of Q^{-1} we obtain:

$$\alpha(\omega) = \sqrt{\frac{\left(\sqrt{1+(Q^{-1})^2}-1\right)}{\left(\sqrt{1+(Q^{-1})^2}+1\right)}} \tag{21}$$

Damping in real soils follows the weak-dissipation assumption such as we could consider $Q^{-1} \ll 1$. Thus, truncating the Taylor of α at the first order yields to the approximation under the weak-dissipation configuration:

$$\alpha \simeq \frac{1}{2} Q^{-1} \tag{22}$$

Since $\hat{M}$ in (19) can be equal to $\hat{\lambda}$ or $\hat{\mu}$, and given (20) it follows that under the weak-dissipation assumption

$$\hat{\mu} = Re(\hat{\mu})(1 - 2i\alpha_\mu) \text{ and } \hat{k}_s = \omega\sqrt{\frac{\rho}{Re(\hat{\mu})}}(1 + i\alpha_\mu) \tag{23}$$

For the sake of simplicity in this work, the material damping ratios are assumed to be the same, i.e., $\alpha_\mu = \alpha_\lambda$. The complex P-wavenumber $\hat{k}_p$ and the complex Poisson's ratio $\hat{\nu}$ are given by (note that the Poisson's ration thus reduce to the real Poisson's ratio):

$$\hat{k}_p = \hat{k}_s\sqrt{\frac{Re(\hat{\mu})}{Re(\hat{\lambda}) + 2Re(\hat{\mu})}}, \quad \nu = Re(\hat{\nu}) = \frac{Re(\hat{\lambda})}{2(Re(\hat{\lambda}) + Re(\hat{\mu}))} \tag{24}$$

It follows that $\alpha_\mu = \alpha_\lambda = \alpha_s$. In practice, to consider weak dissipation, values of attenuation should be contained in the range $0 \leqslant Q^{-1}(\omega) \leqslant 0.2$, which implies $0 \leqslant \alpha(\omega) \leqslant 0.1$. Damping in real soils follows in fact the weak-dissipation assumption, with typical values in the range $\alpha_s \in [0.03, 0.06]$. Table 5 gives the compression rates τ (expressed in thousandths for more readability) for various admissibility conditions and realistic damping ratios α_s. Importantly, after having determined the important parameters for the low frequency case in the previous sections, we can consider a higher frequency ($Re(k_s) = 90$) configuration for this physically sound example.

Table 5 shows that as expected, the compression rate increases with the frequency and with the damping ratio. But the new admissibility condition does not improve the efficiency of the method in this range. We understand at this point that visco-elastodynamic problems are not the most interesting domain of application of the proposed new criterion due to the relatively small damping ratios achieved in real life problems. Hopefully, this approach can be very efficient for purely elastic time-domain problems.

5.2 Efficiency of the approach in the context of the convolution quadrature method for 3D time-domain elastodynamics

Another interesting configuration in which purely elastodynamic problems are consider with a complex wave number is when a CQM-based approach is used to reformulate the time-domain BIE in terms of BIEs in the (complex) frequency domain. The approach can conveniently be presented by focusing on the evaluation of the single-layer integral operator $G\{f\}$ for a given causal density f (see [29] for more details in the context of Helmholtz problems). It is based on a numerical approximation of convolution integrals such as:

$$f * g(x) = \int_0^x f(x-t)g(t)dt, \;\; x \geq 0$$

by quadrature rules. This method has been introduced in [27] where the theoretical procedure to obtain an approximation of a convolution product at discrete times (with constant time step) is obtained and then extended in [26] with variable time steps. [28] gives the numerical evaluation of the quadrature weights. Using the CQM, the influence of the damping in case of visco- or poroelasticity can be taken into account (see [34, 35]). The Z-BEM method refers to the whole solving procedure used here. The use of $\mathcal{Z}$-transform in the context of the CQM eases the approximation of convolution products appearing in the initial time-domain problem. The inverse $\mathcal{Z}$-transform is used to express the discrete time-domain solution obtained once the BIE is solved. This procedure is detailed in an acoustic configuration in [29].

We consider a classical elastodynamic problem in the time-domain. For a given force distribution $\mathbf{F}(\mathbf{y}, t)$ over the geometry studied, an elastodynamic state is any triplet $(\mathbf{u}, \boldsymbol{\sigma}, \mathbf{F})$ satisfying the linear elastic constitutive equation and the fundamental equation of motion

$$\begin{cases} \boldsymbol{\sigma} = \lambda(div\mathbf{u})\mathbf{1} + \mu\left(\nabla\mathbf{u} + \nabla^T\mathbf{u}\right) \\ div\boldsymbol{\sigma} + \rho(\mathbf{F} - \ddot{\mathbf{u}}) = 0 \qquad\qquad \forall(\mathbf{y}, t) \in \Omega \times [0, T] \\ \mathbf{u}(\mathbf{y}, 0) = \mathbf{u}_0(\mathbf{y}) \;\; \dot{\mathbf{u}}(\mathbf{y}, 0) = \mathbf{v}_0(\mathbf{y}) \\ + \text{prescribed boundary conditions} \end{cases} \tag{25}$$

From (25), we deduce the integral representation for an elastodynamic state [5]

$$u_k(\mathbf{x}, t) + \int_{\partial\Omega}\{T_i^k(\mathbf{x}, t, \mathbf{y}) * u_i(\mathbf{y}, t) - U_i^k(\mathbf{x}, t, \mathbf{y}) * t_i(\mathbf{y}, t)\}dS_y = \int_\Omega \rho U_i^k(\mathbf{x}, t, \mathbf{y}) * F_i(\mathbf{y}, t)dV_y$$

$$+ \int_\Omega \rho\{v_{0i}(\mathbf{y})U_i^k(\mathbf{x}, t, \mathbf{y}) + u_{0i}(\mathbf{y})\dot{U}_i^k(\mathbf{x}, t, \mathbf{y})\}dV_y \tag{26}$$

where $T_i^k = \Sigma_{ij}^k n_j$ are the components of the traction vector associated with the fundamental solution. By applying a limiting process [5], we obtain the following regularized displacement integral equation [5]

$$\int_{\partial\Omega}\left[T_i^k(\mathbf{x}, t, \mathbf{y}) * u_i(\mathbf{y}, t) - u_i(\mathbf{x}, t)T_i^k(\mathbf{x}, \mathbf{y})\right]dS_y - \int_{\partial\Omega} U_i^k(\mathbf{x}, t, \mathbf{y}) * t_i(\mathbf{y}, t)dS_y = 0 \tag{27}$$

To present the $\mathcal{Z}$-BEM approach [29] to solve (27) in the time domain we focus on the evaluation of the single-layer integral operator:

$$q(t) = \int_{\partial\Omega} U_i^k(\mathbf{x}, t, \mathbf{y}) * t_i(\mathbf{y}, t) dS_y = \int_{\partial\Omega} \int_0^t U_i^k(\mathbf{x}, t-\tau, \mathbf{y}) * t_i(\mathbf{y}, \tau) d\tau dS_y$$

The starting point is to note that $U_i^k(\mathbf{x}, t-\tau, \mathbf{y})$ may be expressed in terms of its Laplace transform $\bar{U}_i^k$ (assuming it is well-defined), so that for $\mathbf{x}$ and $\mathbf{y}$ fixed:

$$\begin{aligned} q(t) &= \int_0^t \left(\frac{1}{2\pi i} \int_{\gamma-i.\infty}^{\gamma+i.\infty} \bar{U}_i^k(s) e^{s(t-\tau)} ds \right) t_i(\tau) d\tau \\ &= \frac{1}{2\pi i} \int_{\gamma-i.\infty}^{\gamma+i.\infty} \bar{U}_i^k(s) h(\tau; s) ds, \text{ with } h(t; s) := \int_0^t e^{s(t-\tau)} t_i(\tau) d\tau. \end{aligned} \quad (28)$$

Considering a sequence of discrete time instants $t_n = n\Delta t, n \in \mathbb{N}$, where Δt is the constant time step, the CQM is developed as a means to evaluate the sequence $(q_n)_{n\geq 0}$ of convolution values $q_n := q(t_n)$, over a finite discrete time interval $\{0, \Delta t, 2\Delta t \ldots, T = M\Delta t\}$, given the sequence $(t_{i_n}) := (t_i(t_n))_{n\geq 0}$ and the fundamental solution U_i^k. The key point of the CQM consists then in remarking that the function $t \longrightarrow h(t; s)$ introduced in (28) satisfies the initial-value problem:

$$\begin{cases} \frac{dh}{dt}(t; s) = sh(t; s) + t_i(t) \\ h(t \leqslant 0; s) = 0 \end{cases} \quad (29)$$

We can numerically solve the ordinary differential equation (29) for the time-discrete approximation: $h_n(s) := h(t_n, s)$ of $h(t; s)$ (with fixed s) by applying for example a linear multistep method to (29) such that

$$\begin{cases} \frac{dh_n(s)}{dt} \simeq \frac{1}{\Delta t} \sum_{j=0}^k \alpha_j h_{n+j-k}(s) = \sum_{j=0}^k \beta_j (s h_{n+j-k}(s) + t_{i_{n+j-k}}), & \forall n \in \mathbb{N}, \\ h_{-p} = t_{i_{-p}} = 0 & \forall p \in [|1, k|] \end{cases} \quad (30)$$

where the coefficients α_j and β_j are the constants of the multistep method (for instance, $k = 2, \alpha_0 = 1, \alpha_1 = -4, \alpha_2 = 3, \beta_0 = \beta_1 = 0, \beta_2 = 2$ for the Backward Differentiation Formula of order 2 (BDF2) method). The $\mathcal{Z}$-transform $\mathcal{Z}[(x_n)](\xi)$ of a discrete time signal (x_n) is given for $|\xi| \leqslant \varrho$ (with ϱ the radius of convergence of the series) by

$$\mathcal{Z} : (x_n) = \{x_0, x_1, \ldots\} \longrightarrow \mathcal{Z}[(x_n)](\xi) = \sum_{n=0}^{\infty} x_n \xi^n \equiv \mathbf{X}(\xi), \quad \xi \in \mathbb{C} \quad (31)$$

Multiplying by $\Delta t \xi^n$, taking the $\mathcal{Z}$-transform of (30) and taking the sum over n, we obtain after some manipulations

$$\sum_{j=0}^k \alpha_j \xi^{k-j} \mathbf{H}(\xi; s) = \Delta t \sum_{j=0}^k \beta_j \xi^{k-j} (s\mathbf{H}(\xi; s) + \mathbf{T}_i(\xi)) \quad (32)$$

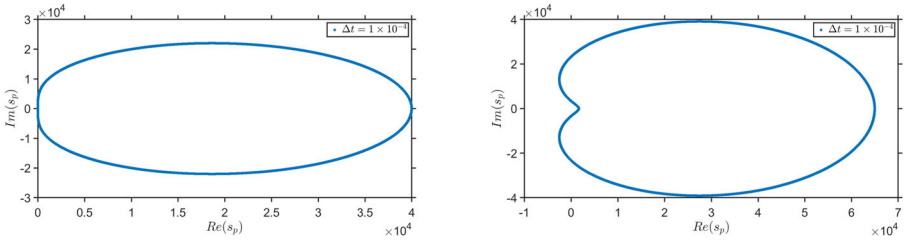

(a) s_p values for the BDF2 linear multistep method

(b) s_p values for the BDF3 linear multistep method

Fig. 15 Complex frequencies s_p for which BEM problems have to be solved in the $\mathcal{Z}$-BEM for two different linear multistep methods and a time step $\Delta t = 10^{-4}$

such that

$$\mathbf{H}(\xi, s) = \frac{1}{\frac{p(\xi)}{\Delta t} - s}\mathbf{T}_i(\xi) \quad \text{with} \quad p(\xi) = \frac{\sum_{j=0}^{k} \alpha_j \xi^{k-j}}{\sum_{j=0}^{k} \beta_j \xi^{k-j}} \tag{33}$$

p is characteristic of the multistep method chosen: $p(\xi) = (3 - 4\xi + \xi^2)/2$ for the BDF2 method and $p(\xi) = (11 - 18\xi + 9\xi^2 - \xi^3)/6$ for the BDF3 method. With the help of the Cauchy's residue theorem, we obtain an approximation of the $\mathcal{Z}$-transform of the convolution product

$$\mathbf{Q}(\xi) = \bar{\mathbf{U}}_i^k \left(\frac{p(\xi)}{\Delta t} \right) \mathbf{T}_i(\xi). \tag{34}$$

We can then extend this result to the whole BIE (27). It involves the numerical resolution of distinct BIEs in the complex frequency domain given by the discrete values of s: $s_p = p(\xi_p)/\Delta t$ with $\xi_p = \rho e^{2i\pi p/L}$, L complex numbers taken on the circle of radius ρ in the complex space. Once the solution $\mathbf{U}_i(., \xi)$ is obtained, the time discrete physical unknowns $u_i(., t_n)$ are obtained by taking the inverse $\mathcal{Z}$-transform of $\mathbf{U}_i(., \xi)$ given by:

$$u_i(., t_n) = \frac{1}{2i\pi} \int_C \mathbf{U}_i(., \xi) \xi^{-k-1} d\xi \simeq \frac{1}{L} \sum_{p=0}^{L-1} \mathbf{U}_i(., \xi_p) \xi_p^{-k}, \quad \forall k \in [|0, M|] \tag{35}$$

with M the total number of time steps. Figure 15 illustrates the complex frequencies s_p at which the solution of the BIE is required for $\Delta t = 10^{-4}$ and for the BDF2 (Fig. 15a) and BDF3 (Fig. 15b) linear multistep methods in (30). Figure 15 illustrates that the $\mathcal{Z}$-BEM implies the solutions of BEM problems with complex wavenumbers for which the decay ratio $\alpha_s = Im(k_s)/Re(k_s)$ is taken in a large range.

Precisely, for our examples with $\Delta t = 10^{-4}$, we obtain $\min \alpha_s = 0$, $\max \alpha_s = 215$ for BDF2 and $\max \alpha_s = 16240$ for BDF3. Due to the definition of s_p, these numbers will increase if Δt is decreased. For each integration contour in Fig. 15, Table 6 gives the number of complex frequencies lying inside some damping ratio intervals. It illustrates the repartition of the interesting damping ratios for this application. Finally, Tables 7 and 8 give the compression rates τ (expressed in thousandths for more readability) for various admissibility conditions and the damping ratios α_s observed in Fig. 15a and b respectively, with the help of Table 6. Our point here is to illustrate

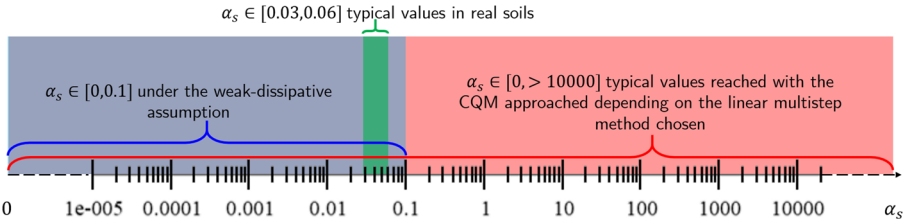

Fig. 16 Values taken by the damping ratio α_s in case of the $\mathcal{Z}$-BEM approach for time-domain elastodynamics and for visco-elastodynamic problems

the effect of the damping ratio on the compression rate on some situations that can be achieved in the context of the CQM. In particular it might seem unrealistic to consider a damping ratio of 10 000; however, Fig. 15a and b demonstrate that it truly occurs. The damping ratio is not the only parameter to take into account, the frequency also has an important impact. To give a good overview of the different situations and understand the general trends, we show the compression rates for a large sampling of damping ratios reached in practice and for two frequencies representative of low and mid-frequencies. We first note that the standard admissibility condition (6) produces similar results than (10b) + (10c). And for these conditions, when the damping ratio increases, we observe that the obtained compression reaches a plateau and then stagnates. Thus, the introduction of more damping does not change the compression rate. On the other hand, the proposed approach with (6) + (9) enables an increase of the gain as the damping ratio increases. This means that the additional compression is obtained by approximating to zero the non-admissible blocks which verify the condition (9). For the largest damping ratios, we notice that the proposed approach enables to divide the storage requirements by a factor up to three. These largest gains are obtained for the largest damping ratios and are conserved as the frequency increases. These results confirm the interest of the proposed approach in the context of $\mathcal{Z}$-BEM.

Previous results in terms of accuracy were limited to low frequency cases. To finish, in Table 9, we report the error introduced by the new admissibility criterion, err_{rel} defined in (15), for four values of damping ratios α_s for the cases $Re(k_s)a = 18$ and $Re(k_s)a = 90$. Importantly, we note that the accuracy is rather stable when the frequency is increased. By extrapolation, one expects to achieve a good accuracy for all possible values of α_s from Table 6. We also report the number of blocks approximated by blocks full of zeros. For the case $Re(k_s)a = 18$, we have a total of 2 242 blocks, 828 of them being non-admissible with the standard admissibility condition. For the case $Re(k_s)a = 90$, we have a total of 69 001 blocks, 22 301 of them being non-admissible with the standard admissibility condition. For these two frequencies, between one quarter and one half of these non-admissible blocks are approximated with the use of the additional admissibility condition.

To sum up, in the context of the $\mathcal{Z}$-BEM, the new admissibility criteria enables important memory and computational savings. From the study on the error introduced by the new admissibility condition, it follows that depending on the accuracy required in the numerical solution, the parameter ε_{decay} may be tuned. An interesting aspect of the method that will be studied in details in a future work will be how each complex

Table 9 Evolution of err_{rel} with respect to the damping ratio and $Re(k_s)a$, $[\varepsilon_{decay} = 10^{-10}]$

Damping ratio	err_{rel} $Re(k_s)a = 18$	Blocks (9) $Re(k_s)a = 18$	err_{rel} $Re(k_s)a = 90$	Blocks (9) $Re(k_s)a = 90$
20	$1.48\ 10^{-9}$	252	$8.83\ 10^{-9}$	5024
30	$1.62\ 10^{-7}$	312	$5.63\ 10^{-8}$	6096
50	$6.16\ 10^{-4}$	354	$2.29\ 10^{-5}$	7452
66	$6.09\ 10^{-4}$	390	$4.05\ 10^{-4}$	8236
100	$3.41\ 10^{-4}$	406	$8.15\ 10^{-3}$	9430
500	$9.36\ 10^{-14}$	426	$1.62\ 10^{-5}$	11126
1000	$< 10^{-16}$	444	$5.32\ 10^{-10}$	11662

frequency contributes to the final accuracy of the purely elastic problem. Thus, they do not contribute equally such that additional savings could be obtained in some ranges.

6 Conclusion

In this work, we have evolved the admissibility condition in the $\mathcal{H}$-BEM to simulate 3D elastodynamic problems with complex wavenumbers. This evolution, which consists in adding condition (9) to the classical condition (6), is a way to obtain improved data-sparse approximations of the discretized Green's tensor. It takes into account the influence of the imaginary part of the complex wavenumbers on the exponential decay induced in the Green's tensor. This exponential decay has a moderate influence on the data-sparse approximation of the matrix in the visco-elastodynamic regime. However it has a much stronger influence on the data-sparse approximation of the matrix in the context of the convolution quadrature method for BEMs 3D elastodynamics. The literature on this topic is so far quite limited. In [12] Börm, Lopez-Fernandez, and Sauter proposed a new admissibility condition to study highly oscillatory Helmholtz kernels with complex wave numbers in the context of directional $\mathcal{H}^2$-matrices. We have shown that our new admissibility condition is simpler to implement and allows one to achieve improved compression rates with a controlled loss of accuracy. We observe that we have used the sound theoretical background proposed in [12] to back up the efficiency of our approach.

It is the authors' belief that the present study could have a real impact on the efficiency of the $\mathcal{Z}$-BEM approach for 3D elastodynamics (and Helmholtz) in the time domain. Among others, we have shown that the gain in terms of memory requirements becomes significant when the damping ratio is above a *threshold value*. In such configurations, the storage requirement converges towards a *minimal* storage representative of non-admissible blocks only. Indeed, the non-admissible blocks have a fixed position in the matrix, and the discretized Green's tensor can be accurately approximated by these non-admissible blocks only, as the strong exponential decay

allows one to approximate all the admissible part of the matrix by matrices of zeros. Figure 16 summarizes the range of values reached by the damping ratio α_s when the $\mathcal{Z}$-BEM approach is used for purely elastic problems and for visco-elastodynamic problems.

Declarations

Conflict of interest The authors declare no competing interests.

References

1. Banjai, L., Hackbusch, W.: Hierarchical matrix techniques for low-and high-frequency Helmholtz problems. IMA J. Numer. Anal. **28**(1), 46–79 (2008)
2. Bebendorf, M.: Hierarchical Matrices. Springer (2008)
3. Bebendorf, M., Kuske, C., Venn, R.: Wideband nested cross approximation for Helmholtz problems. Numer. Math. **130**(1), 1–34 (2015)
4. Bebendorf, M., Rjasanow, S.: Adaptive low-rank approximation of collocation matrices. Computing **70**(1), 1–24 (2003)
5. Bonnet, M.: Boundary Integral Equations Methods in Solids and Fluids. Wiley (1999)
6. Börm, S.: Data-sparse approximation of non-local operators by h2-matrices. Linear Algebra Applic. **422**(2-3), 380–403 (2007)
7. Börm, S.: Directional-matrix compression for high-frequency problems. Numer. Linear Algebra Applic. **24**(6), e2112 (2017)
8. Börm, S., Christophersen, S.: Approximation of integral operators by Green quadrature and nested cross approximation. Numer. Math. **133**(3), 409–442 (2016)
9. Börm, S., Grasedyck, L., Hackbusch, W.: Introduction to hierarchical matrices with applications. Eng. Anal. Bound. Elements **27**(5), 405–422 (2003)
10. Börm, S.: Fast large-scale boundary element algorithms. arXiv:2001.05523 [cs, math] (2020)
11. Börm, S., Börst, C.: Hybrid matrix compression for high-frequency problems. SIAM J. Matrix Anal. Applic. **41**(4), 1704–1725 (2020). Society for Industrial and Applied Mathematics
12. Börm, S., Lopez-Fernandez, M., Sauter, S.A.: Variable order, directional $\mathcal{H}^2$-matrices for Helmholtz problems with complex frequency. IMA Journal of Numerical Analysis, 12. draa046 (2020)
13. Chaillat, S., Bonnet, M.: Recent advances on the fast multipole accelerated boundary element method for 3d time-harmonic elastodynamics. Wave Motion **50**(7), 1090–1104 (2013)
14. Chaillat, S., Desiderio, L., Ciarlet, P.: Theory and implementation of H-matrix based iterative and direct solvers for Helmholtz and elastodynamic oscillatory kernels. J. Comput. Phys. **351**, 165–186 (2017)
15. Ciarlet, P.G.: Introduction to Numerical Linear Algebra and Optimisation. Cambridge University Press (1989)
16. Darve, E.: The fast multipole method: Numerical implementation. J. Comput. Phys. **160**(1), 195–240 (2000)
17. Golub, G.H., Van Loan, C.F.: Matrix Computations, 3rd edn. JHU Press (2012)
18. Grasso, E.: Modelling visco-elastic seismic wave propagation: a fast-multipole boundary element method and its coupling with finite elements. phdthesis. Université Paris-Est (2012)
19. Grasso, E., Chaillat, S., Bonnet, M., Semblat, J.F.: Application of the multi-level time-harmonic fast multipole BEM to 3-D visco-elastodynamics. Eng. Anal. Bound. Elements **36**(5), 744–758 (2012)
20. Greengard, L., Huang, J., Rokhlin, V., Wandzura, S.: Accelerating fast multipole methods for the Helmholtz equation at low frequencies. IEEE Comput. Sci. Eng. **5**(3), 32–38 (1998)
21. Greengard, L., Rokhlin, V.: A fast algorithm for particle simulations. J. Comput. Phys. **73**(2), 325–348 (1987)
22. Hackbusch, W.: A sparse matrix arithmetic based on $\mathcal{H}$-matrices. Part I: Introduction to $\mathcal{H}$-matrices. Computing **62**(2), 89–108 (1999)
23. Hackbusch, W.: Hierarchical Matrices: Algorithms and Analysis, vol. 49. Springer (2015)

24. Hackbusch, W., Nowak, Z.P.: On the fast matrix multiplication in the boundary element method by panel clustering. Numer. Math. **54**(4), 463–491 (1989)
25. Liu, Y.J., Mukherjee, S., Nishimura, N., Schanz, M., Ye, W., Sutradhar, A., Pan, E., Dumont, N.A., Frangi, A., Saez, A.: Recent advances and emerging applications of the boundary element method. Appl. Mech. Rev., 64(3) (2011)
26. Lopez-Fernandez, M., Sauter, S.: Generalized convolution quadrature with variable time stepping. IMA J. Numer. Anal. **33**(4), 1156–1175 (2013). Conference Name: IMA Journal of Numerical Analysis
27. Lubich, C.: Convolution quadrature and discretized operational calculus. I. Numer. Math. **52**(2), 129–145 (1988)
28. Lubich, C.: Convolution quadrature and discretized operational calculus. I II. Numer. Math. **52**(4), 413–425 (1988)
29. Mavaleix-Marchessoux, D., Bonnet, M., Chaillat, S., Leblé, B.: A fast BEM procedure using the Z-transform and high-frequency approximations for large-scale 3D transient wave problems. International Journal for Numerical Methods in Engineering. Wiley (2020)
30. Messner, M., Schanz, M., Darve, E.: Fast directional multilevel summation for oscillatory kernels based on Chebyshev interpolation. J. Comput. Phys. **231**(4), 1175–1196 (2012)
31. Rokhlin, V.: Rapid solution of integral equations of classical potential theory. J. Comput. Phys. **60**(2), 187–207 (1985)
32. Sauter, S.: Variable order panel clustering. Computing **64**(3), 223–261 (2000)
33. Sauter, S.A., Schwab, C.: Boundary element methods. In: Boundary Element Methods, pp. 183–287. Springer (2010)
34. Schanz, M.: Application of 3D time domain boundary element formulation to wave propagation in poroelastic solids. Eng. Anal. Bound. Elem **25**(4), 363–376 (2001)
35. Schanz, M., Antes, H.: A new visco- and elastodynamic time domain boundary element formulation. Comput. Mech. **20**(5), 452–459 (1997)
36. Semblat, J.-F., Luong, M.P.: Wave propagation through soils in centrifuge testing. J. Earthquake Eng. **02**(01), 147–171 (1998). Imperial College Press
37. Wilkes, D.R., Duncan, A.J.: A low frequency elastodynamic fast multipole boundary element method in three dimensions. Comput. Mech. **56**(5), 829–848 (2015)

Affiliations

Laura Bagur[1] · Stéphanie Chaillat[1] · Patrick Ciarlet Jr.[1]

Laura Bagur
laura.bagur@ensta-paris.fr

Patrick Ciarlet Jr.
patrick.ciarlet@ensta-paris.fr

[1] Laboratoire POEMS (CNRS-INRIA-ENSTA Paris), ENSTA Paris, Institut Polytechnique de Paris, 828 Bd des Maréchaux, Palaiseau, 91120, France

AUTHOR QUERIES

AUTHOR PLEASE ANSWER ALL QUERIES:

Q1. "Stéphanie Chaillat" was captured as the corresponding author. Please check if correct.

Q2. Mathematics Subject Classification (2010) is required. Please provide.

Q3. Figures 5, 6, 7, 8, 9, and 16 contains poor-quality text inside the artwork. Please do not re-use the file that we have rejected or attempt to increase its resolution and re-save. It is originally poor; therefore, increasing the resolution will not solve the quality problem. We suggest that you provide us the original format. We prefer replacement figures containing vector/editable objects rather than embedded images. Preferred file formats are eps, ai, tiff, and pdf.

Q4. Figures 4 and 15 contain poor-quality and small text inside the artwork. Please do not re-use the file that we have rejected or attempt to increase its resolution and re-save. It is originally poor; therefore, increasing the resolution will not solve the quality problem. We suggest that you provide us the original format. We prefer replacement figures containing vector/editable objects rather than embedded images. Preferred file formats are eps, ai, tiff, and pdf.

Q5. A citation for Figure 1 is missing. Thus, a citation for Figure 1 was inserted. Please check if appropriate. Otherwise, please provide citation for Figure 1. Note that the order of main citations of figures/tables in the text must be sequential.